Empirical Constraints on the Nucleosynthesis of Nitrogen

James W. Johnson,[1,2][*] David H. Weinberg,[1,2,3] Fiorenzo Vincenzo,[1,2,4] Jonathan C. Bird,[5] and
Emily J. Griffith[1,2]

[1] *Department of Astronomy, The Ohio State University, 140 W. 18th Ave., Columbus, OH, 43210, USA*
[2] *Center for Cosmology and Astroparticle Physics (CCAPP), The Ohio State University, 191 W. Woodruff Ave., Columbus, OH, 43210, USA*
[3] *Institute for Advanced Study, 1 Einstein Dr., Princeton, NJ, 08540, USA*
[4] *E.A. Milne Centre for Astrophysics, University of Hull, Cottingham Rd, Kingston upon Hull, HU6 7RX, United Kingdom*
[5] *Department of Physics & Astronomy, Vanderbilt University, 2301 Vanderbilt Place, Nashville, TN, 37235, USA*

ABSTRACT

We use a multi-ring galactic chemical evolution model to probe the nucleosynthesis of N in the Milky Way. This approach incorporates the effects of stellar migration by allowing stars to move between rings in a manner based on a hydrodynamical simulation. In order to reproduce the gas-phase [N/O]-[O/H] relation, the metallicity dependence of N yields must be approximately linear. The combination of a massive star yield which does not depend on progenitor metallicity with an AGB star yield which does is sufficiently accurate for chemical evolution models. In our model, the [N/O]-[O/H] relation arises not as an evolutionary sequence but as a superposition of endpoints. This occurs because [O/H] reaches equilibrium significantly faster than [N/H], a consequence of the difference in enrichment timescales between the two elements. Our model successfully reproduces many of the observed correlations between stellar N, O, and Fe abundances when their [N/H] measurements are corrected for internal mixing processes known to affect the photospheric compositions of red giant stars. The timescale for N production is significantly shorter than the timescale for stellar migration, and the resulting impact on enrichment rates is minimal. We demonstrate that it is a minimal source of scatter in the gas-phase [N/O]-[O/H] relation as a consequence. Variations in the star formation efficiency and episodic accretion both produce changes in [N/O] at fixed [O/H] that are a factor of ~2 larger than that induced by stellar migration. Our models run using the publicly available `Versatile Integrator for Chemical Evolution` (VICE; https://pypi.org/project/vice).

Key words: methods: numerical – galaxies: abundances, evolution, star formation, stellar content

1 INTRODUCTION

From a nucleosynthesis perspective, N is a unique element. Along with C and He, it is one of only three elements lighter than iron peak nuclei thought to owe a significant portion of their abundances to asymptotic giant branch (AGB) stars (Johnson 2019). N is also the primary by-product of the CNO cycle, a cyclic nuclear reaction which catalyses the conversion of H into He in non-zero metallicity stars more massive than the sun. However, uncertainties surrounding the nucleosynthetic yields of N make it difficult to model its abundances accurately. Here we take an empirical approach to constrain N yields by using state-of-the-art galactic chemical evolution (GCE) models to assess which functional forms describing the yield can reproduce the latest observational data - in particular the new measurements of Milky Way trends by Vincenzo et al. (2021).

Observationally, N abundances in external galaxies are generally measured in the gas phase and are used as a metallicity indicator because of their strong correlation with O abundances. In Fig. 1, we present a compilation of such measurements along with data from the Milky Way:

1. HII regions in the first six CHAOS[1] galaxies: NGC 3184, NGC 628, NGC 5194, NGC 5457, M101, and NGC 2403 (Berg et al. 2020; Skillman et al. 2020; Rogers et al. 2021).
2. HII regions in nearby NGC spirals (Pilyugin, Vílchez & Thuan 2010).
3. HII regions in blue, diffuse star forming dwarf galaxies (Berg et al. 2012; Izotov, Thuan & Guseva 2012; James et al. 2015).
4. Local stars and HII regions (Dopita et al. 2016).
5. Galactic and extragalactic HII regions (Henry, Edmunds & Köppen 2000).
6. Star-forming regions in 550 nearby galaxies in the MaNGA IFU[2] survey (Belfiore et al. 2017).

Despite intrinsic scatter and some systematic variation in how the abundances are determined, this [N/O]-[O/H][3] relation is more or less the same across a wide range of astrophysical environments. Furthermore, recent arguments from both theoretical (Vincenzo &

---

[1] CHAOS: CHemical Abundances Of Spirals (Berg et al. 2015)
[2] MaNGA: Mapping Nearby Galaxies at Apache Point Observatory (Bundy et al. 2015). IFU: Integral Field Unit.
[3] We follow standard notation where $[X/Y] \equiv \log_{10}(X/Y) - \log_{10}(X/Y)_\odot$.
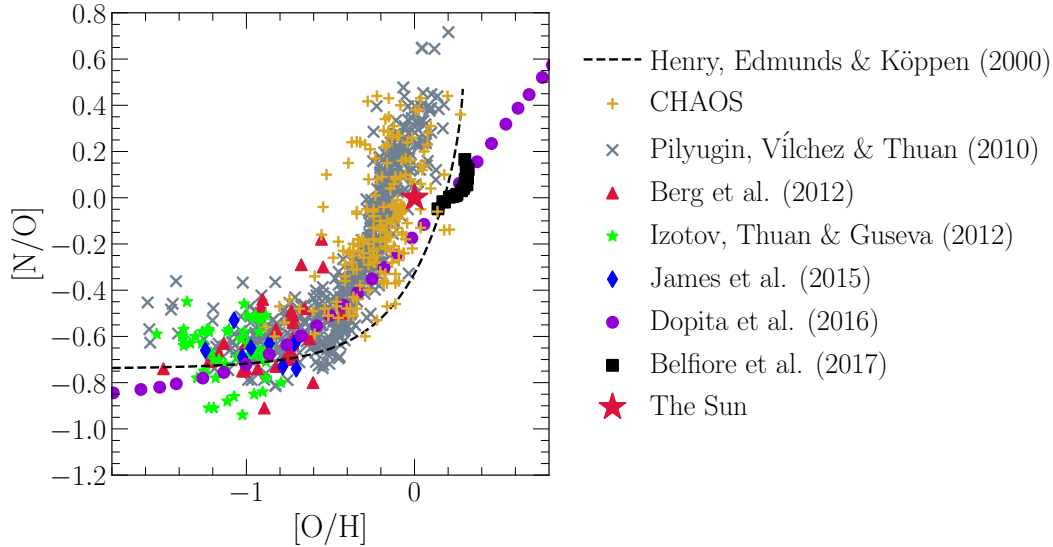
Figure 1. The [N/O]-[O/H] relation as observed in different galactic environments: HII regions from the first six CHAOS galaxies (golden +'s: NGC 3184, NGC 628, NGC 5194, NGC 5457, M101, and NGC 2403; Berg et al. 2020; Skillman et al. 2020; Rogers et al. 2021) and other nearby NGC spiral galaxies (grey X's; Pilyugin et al. 2010), HII regions in blue diffuse star forming dwarf galaxies (red triangles: Berg et al. 2012; green stars: Izotov et al. 2012; blue diamonds: James et al. 2015), in local stars and HII regions (purple circles: Dopita et al. 2016), and in the MaNGA IFU survey (black squares: Belfiore et al. 2017). The fit to [N/O] as a function of [O/H] in Galactic and extragalactic HII regions by Henry et al. (2000) is shown as a black dashed line. We omit all uncertainties for visual clarity. The Sun, at (0, 0) on this plot by definition, is marked by a large red star.

Kobayashi 2018) and observational perspectives (Hayden-Pawson et al. 2021) suggest that this relation is largely redshift-invariant. Previous studies have interpreted this consistency as an indication that the relation is nucleosynthetic in origin, reflective of a "primary" yield which does not depend on a star's initial metal content and a "secondary" yield which does (Vila-Costas & Edmunds 1993; van Zee, Salzer & Haynes 1998; Henry & Worthey 1999; Pérez-Montero & Contini 2009; Pilyugin, Grebel & Mattsson 2012; Andrews & Martini 2013). Both yield components are predicted by stellar evolution models and are ultimately expelled in stellar winds and core collapse supernovae (CCSNe). Although we have highlighted star forming galaxies in Fig. 1, N abundances are also easily measured in massive ellipticals (see, e.g., Schiavon 2010, Conroy 2013, and Conroy, Graves & van Dokkum 2014 for observational references), allowing it to potentially bridge the gap between the physical processes affecting galaxies of different morphologies.

The largest source of uncertainty in understanding N abundances is that accurate and precise nucleosynthetic yields from various enrichment channels remain elusive. Relative to other elements, N is a particularly difficult species to predict yields for in stellar evolution models (see discussion in, e.g., Andrews et al. 2017). In this paper, we constrain N yields empirically by testing the performance of various assumptions within the framework of GCE models. To this end we make use of the multi-zone model for the Milky Way published in Johnson et al. (2021), which treats the Galaxy as a series of concentric rings, describing each one as a conventional one-zone model of chemical evolution (see discussion in § 3). This approach has been employed in the past to compute abundances for many Galactic regions simultaneously (Matteucci & Francois 1989; Wyse & Silk 1989; Prantzos & Aubert 1995; Schönrich & Binney 2009; Minchev, Chiappini & Martig 2013, 2014; Minchev et al. 2017; Sharma, Hayden & Bland-Hawthorn 2021). Because of the apparent universality of the [N/O]-[O/H] relation, our results using the Milky Way as a case test should apply to other galaxies as well.

Recently, Grisoni, Matteucci & Romano (2021) argued that rotating massive stars play a key role in establishing the N abundances seen in metal-poor stars in the Milky Way. Rotation has a considerable impact on the N yields of massive stars, because the internal mixing that it causes (Zahn 1992; Maeder & Zahn 1998; Lagarde et al. 2012) brings internally produced C and O nuclei into the H-burning shell where they can be processed into ^{14}N via the CNO cycle (Heger & Woosley 2010; Frischknecht et al. 2016; Andrews et al. 2017). We find similar results here comparing various theoretical models for massive star nucleosynthesis (see discussion in § 2.1).

Theoretical models for AGB star nucleosynthesis predict N yields to vary as a function of progenitor mass and metallicity (Cristallo et al. 2011, 2015; Karakas 2010; Karakas & Lugaro 2016; Karakas et al. 2018; Ventura et al. 2013, 2014, 2018, 2020). In sufficiently massive AGB stars, the base of the convective envelope is hot enough to activate proton capture reactions, allowing the CNO cycle to convert C and O isotopes in ^{14}N: a process known as hot bottom burning. AGB stars are also known to experience thermal pulsations, and often these pulations are accompanied by a penetration of the convective enevelope into the CO-rich core, which incorporates some of this material into the envelope itself: a process known as third dredge-up. When both processes are active, third-dredge up adds new seed nuclei for hot bottom burning to turn into ^{14}N, substantially increasing the N yields. We demonstrate in §§ 2.2 and 2.3 that various published theoretical models predict significantly different N yields for high mass AGB stars as a consequence of how third dredge-up and hot bottom burning occur in the models. The differences in these processes are in turn a consequence of the uncertain microphysical assumptions built into the stellar evolution models (e.g. mass loss, opacity, convection and convective boundaries, nuclear reaction networks). In § 4.2, we test the extent to which each of these "off-the-shelf" yield models are able to reproduce the [N/O]-[O/H] relation in GCE models.

In a sample of 6,507 galaxies from the MaNGA IFU survey (Bundy et al. 2015), Schaefer et al. (2020) demonstrate that the intrinsic scat-

ter in the [N/O]-[O/H] relation at fixed galaxy mass is correlated with variations in the local star formation efficiency (SFE). In regions of slower star formation, [N/O] tends to be slightly higher at fixed [O/H] (see their Fig. 4), which is expected from simple GCE models. In classical "closed-box models" (e.g. Mollá et al. 2006), more AGB stars enrich the ISM with N by the time a given [O/H] is reached, whereas in "open-box models" with inflows and outflows like the ones we present here, dilution by primordial gas accretion drives [O/H] down at fixed [N/O]. However, Schaefer et al. (2020) did not rule out stellar migration as an additional source of scatter in the gas-phase [N/O]-[O/H] relation. In principle, there could be a deficit or surplus of N-producing AGB stars in a given Galactic region at any time simply because the orbits are evolving, driving additional scatter in the correlation. The Johnson et al. (2021) GCE model is the ideal tool with which to test this hypothesis; the novel difference between theirs and previous models with similar motivations is that it allows stellar populations to enrich distributions of radii as they migrate. Originally developed to study the abundances of O and iron (Fe), this aspect of Galactic evolution turned out to have an important impact on the delayed type Ia supernova (SN Ia) enrichment of Fe, causing stochastic fluctuations in the enrichment rates with time at fixed radius. Here we use the same methodology to test for similar effects in the delayed AGB star production of N, in turn assessing whether migration or variability in the SFE dominate scatter in the [N/O]-[O/H] relation.

With stellar abundance data, we can test the N abundances predicted by our model against observables unavailable for the gas phase, such as age and [O/Fe]. Using data from the Apache Point Observatory Galaxy Evolution Experiment (APOGEE; Majewski et al. 2017), Vincenzo et al. (2021) demonstrate that when stellar N abundances are corrected for internal mixing processes, the correlations with stellar age and other elemental abundances are affected. Whether or not our GCE model is able to reproduce their corrected data constitutes a valuable test not only of our understanding of N nucleosynthesis, but also the accuracy of the Vincenzo et al. (2021) measurements which take a model-dependent approach to estimate the birth abundances of N for APOGEE red giant disc stars with asteroseismic mass measurements. They find good agreement between the APOGEE abundances and the Dopita et al. (2016) data, which we find to be a good representation of external galaxies as well (see Fig. 1); we therefore take the Dopita et al. (2016) measurements as our observational benchmark.

In § 2, we discuss our adopted yields of N from its dominant nucleosynthetic sources. We discuss the details of our multi-zone chemical evolution model in § 3. We describe the evolution of a fiducial model in § 4.1. In § 4.2, we quantify the [N/O]-[O/H] relation predicted by our model with various "off-the-shelf" AGB star yield models taken from the literature. We investigate the relative importance of the delay-time distribution and the metallicity-dependence of AGB star yields in § 4.3. We compare our model predictions to stellar N abundances corrected for internal mixing processes in § 4.4. Lastly, we assess the sources of intrinsic scatter in the [N/O]-[O/H] relation in § 4.5.

2 NUCLEOSYNTHESIS

Here we make use of the chemical evolution model for the Milky Way presented in Johnson et al. (2021), which runs using the publicly available Versatile Integrator for Chemical Evolution (VICE, see Appendix A; Johnson & Weinberg

2020; Griffith et al. 2021a; Johnson et al. 2021), an opensource PYTHON package designed for GCE modeling. Johnson et al. (2021) focus their discussion of the model predictions on O and Fe, and we retain their yields of these elements here. The supernova (SN) yields are defined as the net mass of some element X produced over all explosion events in units of the progenitor cluster's mass. For example, with a yield of $y_X = 0.001$, a hypothetical 1000 $M_\odot$ star cluster would produce 1 $M_\odot$ of the element X instantaneously in the case of CCSNe or over the delay-time distribution (DTD) in the case of SNe Ia. These yields are net yields in that they do not quantify the metal mass ejected to the interstellar medium (ISM) that was initially present within a star; in the previous example, the 1 $M_\odot$ yield is only the newly produced metal mass. We adopt the following values from Johnson et al. (2021), who in turn base them off of Weinberg, Andrews & Freudenburg (2017) and Johnson & Weinberg (2020):

- $y_O^{CC} = 0.015$
- $y_{Fe}^{CC} = 0.0012$
- $y_O^{Ia} = 0$
- $y_{Fe}^{Ia} = 0.00214,$

where the subscripts and superscripts differentiate between the element and the SN type. We explore variations of these values in the context of the overall normalization of nucleosynthetic yields and Galactic outflows in § 4.2. We assume that N is not produced in significant amounts by SNe Ia (Johnson 2019), setting $y_N^{Ia} = 0$ throughout this paper accordingly, and spend the remainder of this section discussing the CCSN and AGB star yields of N.

A significant portion of N yields arise as a consequence of the CNO cycle.[1] As the dominant source of pressure and energy generation in non-zero metallicity main sequence stars with initial masses of $\gtrsim 1.3\,M_\odot$, this cyclic nuclear reaction catalyses the conversion of H into He that would otherwise be accomplished by the proton-proton chain (Suliga, Shalgar & Fuller 2021). Its slowest component by far is the $^{14}N(p, \gamma)^{15}O$ reaction (e.g. LUNA Collaboration et al. 2006). Consequently, the first order effect of the CNO cycle is to convert most of the C isotopes in stellar cores into ^{14}N. As we will discuss in this section, this plays an important role in shaping N yields from stars of all masses.

## 2.1 Core Collapse Supernovae and Massive Star Winds

In VICE, CCSN nucleosynthetic products are approximated to be produced instantaneously following an episode of star formation; this is a valid approximation due to how short the lives of massive stars are compared to the relevant timescales for GCE. Based on this and its definition as being in units of a stellar population's total mass, the yield is simply the constant of proportionality between the CCSN production rate and the star formation rate (SFR):

$$\dot{M}_X^{CC} = y_X^{CC} \dot{M}_\star \qquad (1)$$

More generally, y_X^{CC} quantifies *all* of the nucleosynthetic material approximated to be produced instantaneously following a single stellar population's formation.

We compute theoretically predicted values of y_N^{CC} using VICE's vice.yields.ccsne.fractional function assuming a Kroupa (2001) IMF; details on how VICE handles these calculations can be found in § 4 of Griffith et al. (2021a) and in

---

[1] $^{12}C(p, \gamma)^{13}N(\beta^+ \nu_e)^{13}C(p, \gamma)^{14}N(p, \gamma)^{15}O(\beta^+ \nu_e)\,^{15}N(p, \alpha)^{12}C$
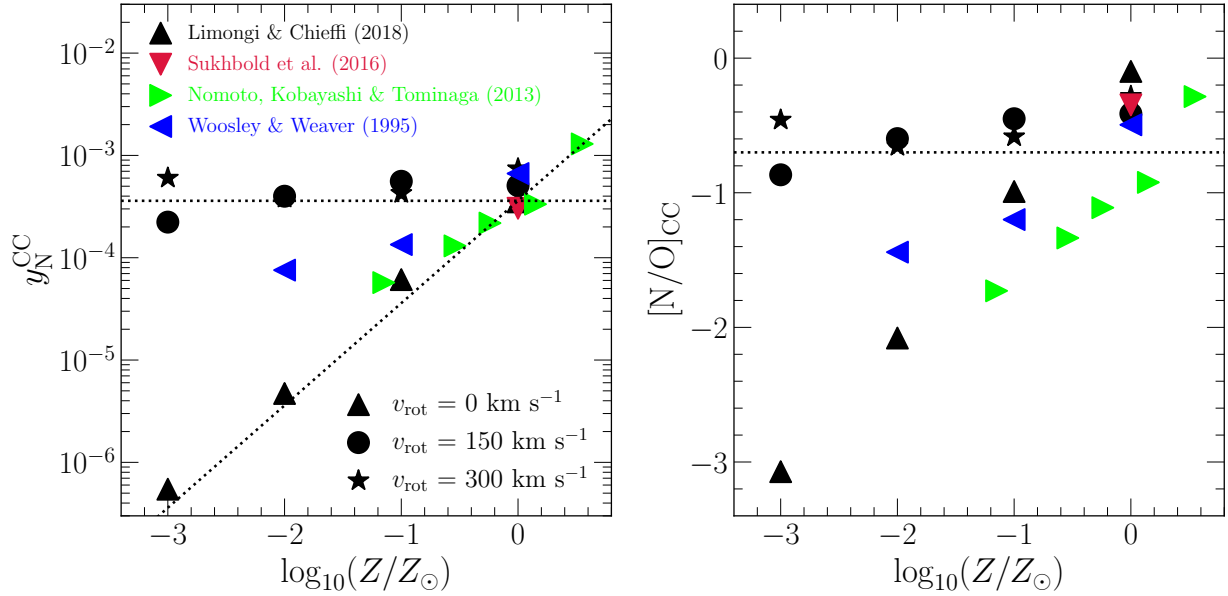
Figure 2. Left: IMF-averaged CCSN yields of N calculated using `VICE`'s `vice.yields.ccsne.fractional` function with the tables published by Woosley & Weaver (1995, blue), Nomoto et al. (2013, green), Sukhbold et al. (2016, red), and Limongi & Chieffi (2018, black). All studies report yields for non-rotating progenitors, shown by the triangles; for visual clarity, the triangles point in a different direction for each study according to the legend. Limongi & Chieffi (2018) report additional yields for progenitors with rotational velocities of 150 (circles) and 300 km/s (stars). The horizontal dashed line marks $y_N^{CC} = 3.6 \times 10^{-4}$, the value of our fiducial CCSN yield of N in our GCE models. We use the form shown by the slanted line (equation 8) in § 4.2.2 in combination with some of our AGB star yield models discussed in § 2.2. **Right**: The [N/O] ratio predicted by each of the explosion models in the left-hand panel, under the same colour-coding and marker scheme. We mark the position of [N/O] = −0.7 with a black dotted line, the value roughly suggested by the observations of low-metallicity systems highlighted in Fig. 1.

the `VICE` science documentation[2]. In the left panel of Fig. 2, we plot the results as a function of progenitor metallicity as predicted by the Woosley & Weaver (1995), Nomoto, Kobayashi & Tominaga (2013), Sukhbold et al. (2016), and Limongi & Chieffi (2018) tables. There is good agreement between the various non-rotating models, but only Limongi & Chieffi (2018) report yields for progenitors with non-zero rotational velocities; these yields are substantially larger than their non-rotating counterparts, especially at low metallicity. With few seed nuclei for the CNO cycle at low Z, production of ^{14}N is difficult. Rotation-induced mixing, a highly uncertain process (Zahn 1992; Maeder & Zahn 1998; Lagarde et al. 2012), could transport newly produced C and O into the hydrogen burning shell of the CCSN progenitor, facilitating ^{14}N production (Frischknecht et al. 2016; see also discussion in § 4.2 of Andrews et al. 2017). Consequently, N yields at low metallicity are quite sensitive to model-dependent assumptions regarding stellar rotation and internal mixing processes (Heger & Woosley 2010).

We compute the [N/O] ratio of CCSN ejecta from the values of y_N^{CC} and y_O^{CC} predicted by a given yield table according to

$$[N/O]_{cc} = \log_{10}\left(\frac{y_N^{CC}}{y_O^{CC}}\right) - \log_{10}\left(\frac{Z_{N,\odot}}{Z_{O,\odot}}\right), \qquad (2)$$

where $Z_{X,\odot}$ is the abundance by mass of some element X in the sun, for which we take $Z_{N,\odot} = 6.91 \times 10^{-4}$ and $Z_{O,\odot} = 5.72 \times 10^{-3}$ based on the photospheric measurements of Asplund et al. (2009). For each value of y_N^{CC} in the left panel of Fig. 2, we compute the

corresponding values of y_O^{CC} and illustrate the resultant [N/O]$_{cc}$ ratios in the right panel. These yield ratios follow similar trends with progenitor metallicity and rotation as y_N^{CC} itself, a consequence of the fact that these studies predict relatively metallicity- and rotation-independent O yields. If we assume [N/O]$_{cc}$ = −0.7 as suggested by Fig. 1 and our adopted O yield of $y_O^{CC} = 0.015$, equation (2) suggests that $y_N^{CC} = 3.6 \times 10^{-4}$. We highlight both [N/O]$_{cc}$ = −0.7 and $y_N^{CC} = 3.6 \times 10^{-4}$ with horizontal black dashed lines in Fig. 2, finding good agreement with the rotating progenitor models of Limongi & Chieffi (2018) in both panels. This suggests that rotating massive stars play an important role in establishing N abundances at low metallicity as recently suggested by Grisoni et al. (2021). We therefore take $y_N^{CC} = 3.6 \times 10^{-4}$ as our fiducial CCSN yield of N; both the normalization and metallicity-independence of this choice are supported by the Limongi & Chieffi (2018) models.

The Sukhbold et al. (2016) tables, available only at solar metallicity, agree nearly perfectly with our empirical value of $y_N^{CC} = 3.6 \times 10^{-4}$, but they overpredict [N/O]$_{cc}$ by ∼0.2 dex. This is a consequence of the failed supernovae incorporated into their model and the lowered values of y_O^{CC} that result (see discussion in § 4.2). While N emerges in substantial amounts in winds, much of the O produced by massive stars is ejected during the explosion, making the O yield more sensitive to the black hole landscape (Griffith et al. 2021a). Although most of the SN models plotted in Fig. 2 slightly overestimate our empirical value of [N/O]$_{cc}$ = −0.7, they still fall short of solar. This implies the need for an additional enrichment channel, which is expected because it is well understood that N is also produced in considerable amounts by AGB stars (Johnson 2019).

---

[2] https://vice-astro.readthedocs.io/en/latest/science_documentation/yields
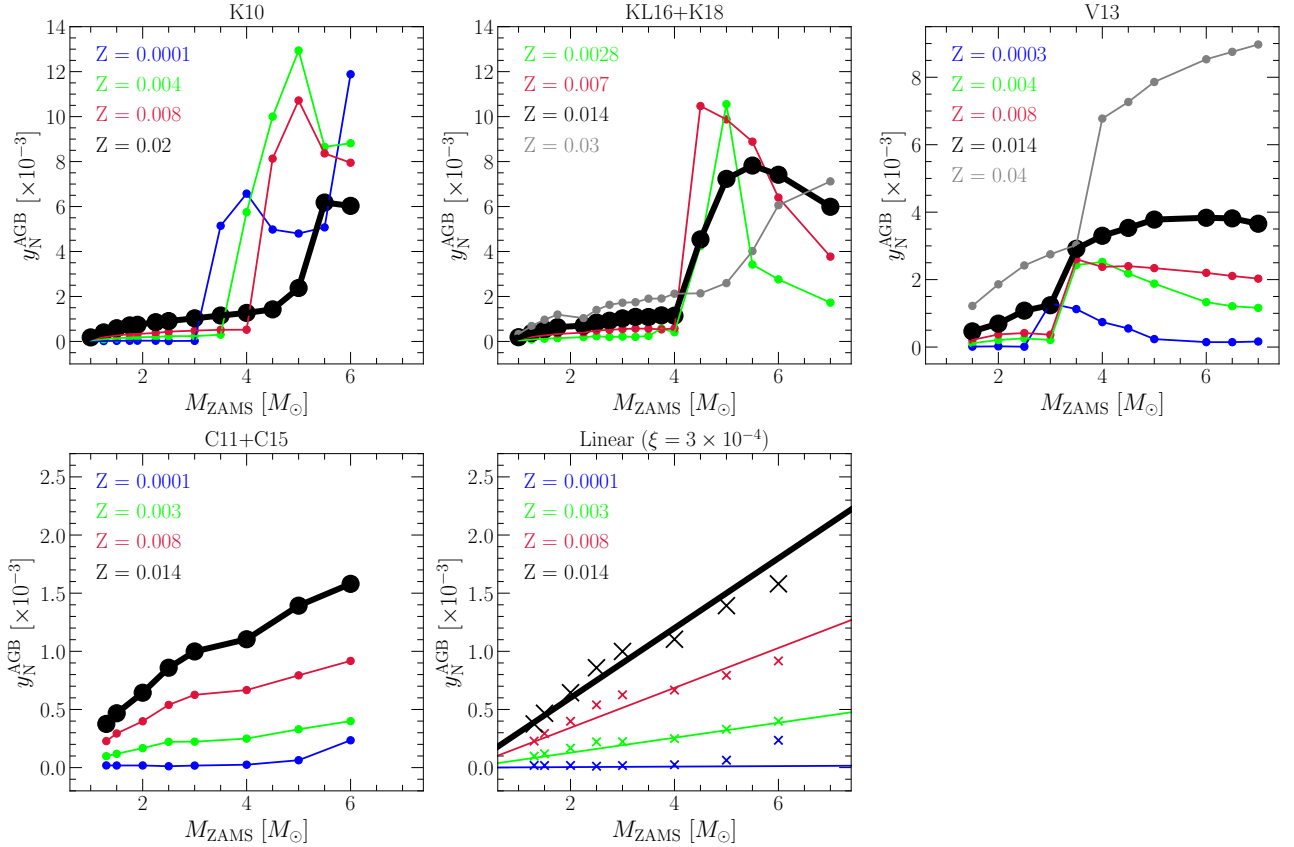
Figure 3. The fractional yields of N from AGB stars y_N^{AGB} as a function of progenitor ZAMS mass and birth metallicity Z as reported by Karakas (2010, upper left), Karakas & Lugaro (2016) and Karakas et al. (2018, upper middle), Ventura et al. (2013, 2014, 2018, 2020, upper right), and Cristallo et al. (2011, 2015, lower left). For Ventura et al. (2013, 2014, 2018, 2020) and Cristallo et al. (2011, 2015), we show the yields only for a selection of metallicities available from their provided tables. We highlight yields at solar metallicity ($Z = 0.02$ for Karakas 2010, $Z = 0.014$ otherwise) with bold black lines. In the lower right panel, we show the yields predicted by our linear model (coloured lines, see equation 3) in comparison to the Cristallo et al. (2011, 2015, coloured X's) predictions. We caution that the axis ranges are not the same between panels in this figure.

2.2 Asymptotic Giant Branch Stars

Similar to SNe, our AGB star yields are parameterized as fractional net yields. For a yield y_X^{AGB}, the mass yield is given by $M_\star y_X^{AGB}$. Enrichment proceeds as it does in Johnson et al. (2021) under the caveat that AGB stars place their nucleosynthetic products in the $\delta R_{gal} = 100$ pc ring that they are in at a given time, allowing stars to enrich distributions of radii as they migrate. In short, VICE implements an algorithm which computes the mass in dying stars from each stellar population, and the zero age main sequence (ZAMS) mass required to compute the fractional yield comes from a mass-lifetime relationship. For the latter, we adopt the metallicity independent parabola in $\log\tau - \log m$ space from Larson (1974) with updated coefficients from Kobayashi (2004) and David, Forman & Jones (1990) throughout this paper (see discussion of the mass-lifetime relationship in VICE in Appendix A).

Here we make use of four previously published tables of AGB star yields computed from stellar evolution models, each of which are sampled on a grid of progenitor masses and metallicities. To approximate the net yield y_X^{AGB} as a smooth function of $M_\star$ and $Z_\star$, VICE interpolates bi-linearly - once in mass and once in metallicity - linearly extrapolating above or below the grid in either quantity as necessary. By comparing the predicted abundances of the Johnson et al. (2021) Milky Way model to the latest observational data,

we can constrain how accurately these "off-the-shelf" yield models characterize N production. These models taken from the literature are:

1. Karakas (2010, hereafter K10)[3] published yields for $Z = 0.0001$, 0.004, 0.008, and 0.02 progenitors. We plot these yields in the upper left panel of Fig. 3.

2. Karakas & Lugaro (2016) and Karakas et al. (2018) published yields for $Z = 0.0028$, 0.007, 0.014, and 0.03 progenitors; we hereafter refer to these yields as the KL16+K18 model. We illustrate these yields in the upper middle panel of Fig. 3.

3. We combine the yields for $Z = 0.0003$ and 0.008 progenitors from Ventura et al. (2013) with those at $Z = 0.004$ from Ventura et al. (2014), at $Z = 0.014$ from Ventura et al. (2018), and at $Z = 0.04$ from Ventura et al. (2020) into a single table of yields. In this set, we also include a set of un-published yields at $Z = 0.001$ and 0.002 computed from similar models (provided by P. Ventura, private communication). We hereafter refer to this yield set as the V13 model, and we plot a subsample of these yields in the upper right panel of Fig. 3.

---

[3] We clarify that our abbreviations of each of these papers refer specifically to their yields of N as we adopt them in our model. We cite the full names of these papers when referring to their more general results.

4. The default set of AGB star yields in `VICE` is taken from Cristallo et al. (2011, 2015), who published yields for $Z = 0.0001, 0.0003, 0.001, 0.002, 0.003, 0.006, 0.008, 0.01, 0.014$, and 0.02 progenitors. We hereafter refer to these yields as the C11+C15 model, and we illustrate a subsample of them in the lower left panel of Fig. 3.

`VICE` also allows users to construct their own functions of progenitor mass and metallicity to describe the AGB star yield. Motivated by the roughly linear nature of the C11+C15 yields and their general success once renormalized by a constant factor (see discussion in § 4.2), we construct a model in which the yield is linearly proportional to both progenitor ZAMS mass and metallicity:

$$y_N^{AGB} = \xi \left(\frac{M}{M_\odot} \right) \left(\frac{Z}{Z_\odot} \right). \tag{3}$$

We illustrate this model in the lower middle panel of Fig. 3 for $\xi = 3\times10^{-4}$ in comparison to the C11+C15 yields shown by the coloured X's. Although we find good agreement between the C11+C15 yields and our linear model with a slope of $\xi = 3 \times 10^{-4}$, for our fiducial AGB star yield of N we take a slope of $\xi = 9 \times 10^{-4}$. We discuss the absolute scaling of our nucleosynthetic yields in § 4.2 below.

Despite reporting values of the same physical quantities, the N yields reported by each of these studies show substantial differences between one another. Unfortunately, ascertaining the origins of their inconsistencies is difficult because each model employs its own assumptions for important evolutionary parameters such as opacity, mass loss, nuclear reaction networks, and convection and convective boundaries within stars, all of which have a significant impact on stellar evolution and thus the predicted yields (see discussion in, e.g., § 5 of Karakas & Lugaro 2016). However, the differences can be qualitatively understood by considering two important phenomena known to occur within AGB stars: third dredge-up[4] (TDU) and hot bottom burning (HBB). The variations in how TDU and HBB proceed between different stellar evolution models arise as consequences of the different input physics.

When an AGB star experiences a thermal pulsation, this is usually accompanied by a TDU event whereby the convective envelope penetrates into the hydrogen-depleted core, mixing some of this material with other material exposed to partial He-shell burning. This process does not affect N abundances much because at this evolutionary phase, the core is mostly composed of C and O. However, the $^{13}C(\alpha, n)^{16}O$ reaction can occur at substantial rates when the core material is mixed with the He-rich shell. This reaction is the main source of free neutrons in low mass AGB stars (Gallino et al. 1998), and as a consequence, each replenishment of C by TDU indirectly raises an AGB star's overall yield. HBB refers to proton capture reactions at the base of the convective envelope, activating the CNO cycle and producing large amounts of ^{14}N at the expense of C and O isotopes. HBB requires a higher mass AGB star progenitor ($M_{ZAMS} = 4 - 5 \, M_\odot$ at $Z_\odot$ according to Karakas 2010) than TDU ($M_{ZAMS} = 2 - 2.5 \, M_\odot$ at $Z_\odot$ according to Karakas 2010), but the minimum mass for both decreases at lower metallicities.

The most efficient N production occurs when both TDU and HBB are active within an AGB star, because each replenishment of C and O isotopes by TDU adds new seed nuclei for the CNO cycle with HBB. This is the reason for the substantial increase in yields

at ~4 $M_\odot$ in the K10 and KL16+K18 models; in both yield sets, every star that experiences HBB also experiences TDU (see, e.g., Table 1 of Karakas 2010). Their high mass AGB star yields are higher at low Z because both HBB and TDU are more efficient (Ventura et al. 2013, see discussion in). When the metallicity is low, each TDU episode is deeper due to the lower opacity, and the base of the convective envelope is hotter, increasing the rate of CNO cycle reactions in HBB. This interaction between TDU and HBB is also the reason for the increase in the V13 yields near ~3 $M_\odot$, but unlike the K10 and KL16+K18 models, their stars experience both processes only in this narrow range of mass.

Of all of these yields taken from the literature, the C11+C15 sample shows the smoothest dependence on progenitor mass and metallicity. Below ~3 $M_\odot$, their agreement with the KL16+K18 yields is good, but this model has much lower N yields for higher mass AGB stars. Even when collapsing the information into TDU and HBB, pinpointing a single reason for this difference is difficult. Relative to the KL16+K18 yields (see discussion in § 5 of Karakas & Lugaro 2016), the C11+C15 stars have more mass loss, fewer thermal pulses overall, and weaker HBB due to a lower temperature at the base of the convective envelope, each of which act to lower the yield of ^{14}N.

Although both the K10 and KL16+K18 yield models both show a substantial increase in N yields above ~4 $M_\odot$, there are some noteworthy differences between the two. In the newer version, the yields at solar metallicity are somewhat higher, and the yields at subsolar metallicities decreased slightly, particularly for the highest mass AGB stars. These differences can be understood by slight variations in the input physics (A. Karakas, private communication). A portion of the increase in the yields at solar metallicity can be attributed to the assumption of $Z_\odot = 0.02$ versus $Z_\odot = 0.014$[5] and the impact this has on both HBB and TDU, but it does not account for the entire difference. As a consequence of updates to opacity tables and the adopted solar composition, the KL16+K18 models at solar metallicity are slightly hotter and more compact, giving them hotter HBB and deeper TDU. With more thermal pulses overall and therefore a longer AGB lifetime, these stars have more time to convert ^{12}C into ^{14}N. KL16+K18 also use low-temperature opacity tables based on Marigo (2002) that more closely follow the surface composition of the star. These opacities are high, making the stars larger and increasing the mass-loss rate relative to K10, truncating the N yield of the highest mass AGB stars. The $Z = 0.0028$ model uses the Bloecker (1995) mass-loss prescription rather than that of Vassiliadis & Wood (1993), which was used for the K10 yields as well as the yields at other metallicities in the KL16+K18 model. This choice results in fewer thermal pulses and a shorter AGB lifetime, giving them less time to process C and O nuclei into ^{14}N.

In the interest of consistency, when we adopt a particular AGB star yield model for N, we also adopt the corresponding table within `VICE` for O and Fe when possible.[6] These O and Fe yields, however, are negligible compared to their SN yields. Although we focus our investigation on AGB yields from $\lesssim 7 \, M_\odot$ stars, slightly more

---

[4] Here the time adverbial "third" refers only to the fact that these dredge-up episodes are occurring while the star is on the asymptotic giant branch. Because they are associated with the thermal pulsations of AGB stars, there are many episodes of third dredge-up.

[5] Changes in the accepted value of the metallicity of the sun trace back to the canonical value of ~2% derived by, e.g., Anders & Grevesse (1989) and Grevesse & Sauval (1998), later being revised to ~1.4% by, e.g., Lodders (2003) and Asplund, Grevesse & Sauval (2005). See Table 4 of Asplund et al. (2009) for a compilation of measured values.

[6] In the case of Ventura et al. (2013, 2014, 2018, 2020), AGB star yields of Fe are not available, and our linear model is only appropriate for N. In these cases, we assume the `VICE` default of the Cristallo et al. (2011, 2015) yields for both O and Fe.
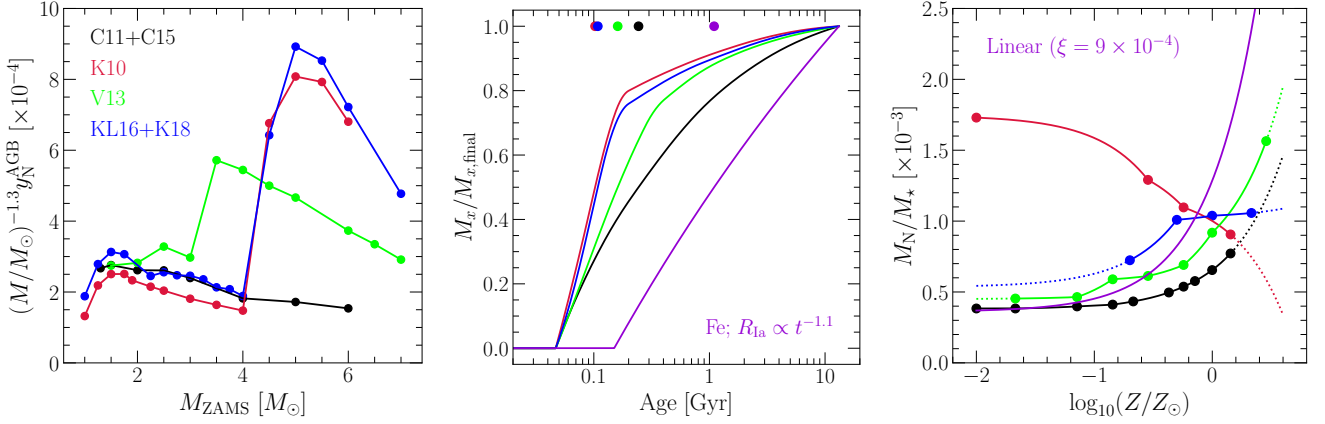
Figure 4. Left: The IMF-weighted mass yield of N from AGB stars as a function of progenitor ZAMS mass at solar metallicity (i.e. the contribution per linear interval dM_{ZAMS}; $Z_\odot = 0.014$). **Middle**: The net mass of N produced by AGB stars from a single stellar population for each of our yield models at solar metallicity. The purple line denotes the same for Fe assuming our $t^{-1.1}$ DTD as in the Johnson et al. (2021) chemical evolution model. All values are normalized to the total mass produced at an age of 13.2 Gyr. Points at the top of the panel denote the ages at which 50% of the total mass yield has been produced. **Right**: The total amount of N produced by a 13.2 Gyr old stellar population as a function of metallicity for each of our yield models normalized by the stellar population's initial mass. Points mark metallicities at which the published tables report yields, and the lines are dotted at metallicities that are above (below) the maximum (minimum) metallicity reported by a given study (i.e. where extrapolation is necessary).

massive stars (up to ~12 $M_\odot$) sit near the critical mass boundaries between different types of massive white dwarfs and electron capture SN progenitors. Doherty et al. (2017) investigated theoretically predicted yields of these stars and found significant production of CNO isotopes. There is also the intriguing possibility of the CNO yields from the earliest, most metal-poor AGB stars (e.g. the $Z = 10^{-5}$ models of Gil-Pons et al. 2013, 2021) and the insight this may afford into N production at low Z and the most metal-poor stars in the Galaxy. While experiments with such yields in our GCE models would be interesting, this is beyond the scope of the current paper since our AGB yield models already span a wide range of assumptions regarding stellar evolution.

2.3 IMF-Averaged AGB Star Yields: Metallicity and Time Dependence

To more directly compare these AGB star yields predicted from stellar evolution models, we plot their IMF-weighted yields at solar metallicity in the left hand panel of Fig. 4. We assume $Z_\odot = 0.014$ based on Asplund et al. (2009) and Asplund, Amarsi & Grevesse (2021); since the K10 model reports yields at $Z = 0.02$ rather than $Z = 0.014$, we simply interpolate linearly to $Z = 0.014$ in the same manner that VICE does in our GCE models. As mentioned in § 2.2, the AGB star yield y_N^{AGB} as we have parameterized it is in units of the progenitor star's ZAMS mass, and consequently the *mass yield* of N is given by $M_\star y_N^{AGB}$. With an additional weight of $M_\star^{-2.3}$ from the IMF in this mass range (e.g. Kroupa 2001), we therefore multiply the values of y_N^{AGB} by $(M_\star/M_\odot)^{-1.3}$ to quantify a star's relative contribution to the total N yield taking into account the intrinsic mass distribution[7] Even with the additional weight of $M_\star^{-1.3}$, the C11+C15 yields are relatively mass-independent. For the other yield models, the contributions from higher mass AGB stars is yet more pronounced due to the effects of TDU and HBB discussed in § 2.2.

---

[7] This weight gives a contribution per linear interval of M_{ZAMS}, so one can use area under the curve to assess relative contributions.

Using VICE's `vice.single_stellar_population` function, in the middle panel of Fig. 4 we plot the total N yield as a function of age from a single stellar population. For the sake of this calculation, we set all CCSN yields of N to zero in order to highlight the AGB star contribution. We show the results of this procedure for solar metallicity only (again $Z = 0.02$ for K10, $Z = 0.014$ otherwise), and we normalize all values to the total mass produced at $T = 13.2$ Gyr (the total amount of time our GCE model is integrated over; see discussion in § 3). Under the C11+C15 yields, it takes ~250 Myr for a single stellar population to produce ~50% of its N from AGB stars, as noted by the coloured points at the top of the panel. This is in good agreement with Maiolino & Mannucci (2019), who find that similar parameter choices predict 80% of the N yield to be ejected within ~1 Gyr (see their Fig 1). The characteristic timescales for N production are even shorter in our alternate yield models with more pronounced contributions from massive stars due to their short lifetimes (e.g. Larson 1974; Maeder & Meynet 1989; Padovani & Matteucci 1993). For comparison, we plot the enrichment of Fe by our $t^{-1.1}$ power-law DTD, also with the CCSN yield set to zero to highlight the delayed component. The characteristic delay time for Fe production is considerably longer than that of N - up to an order of magnitude depending on which yield model is adopted. As noted in Johnson et al. (2021), a characteristic delay time of ~1 Gyr is exactly as expected for a $\sim t^{-1}$ DTD because half of the SN Ia events occur between 100 Myr and 1 Gyr and the other half between 1 Gyr and 10 Gyr.

A characteristic delay time of only ~250 Myr may seem surprising given the relatively mass-independent nature of the IMF-weighted C11+C15 yields. This arises out of the steep nature of the stellar mass-lifetime relation (e.g. Larson 1974; Maeder & Meynet 1989; Padovani & Matteucci 1993). For example, 2 and 3 $M_\odot$ stars live only ~1.2 Gyr and ~400 Myr, respectively, and over the course of 13.2 Gyr, only stars of masses $\gtrsim 0.9$ $M_\odot$ will have enough time to finish their hydrogen burning. Consequently, most of the mass range of stars that will evolve through an AGB phase will do so within the first few hundred Myr after their formation, and with mass-independent IMF-weighted yields, this accounts for most of the N. We clarify that the delay times computed here apply *only* to N

and not necessarily to other elements produced by AGB stars. As we have illustrated here, the effective DTD of AGB star enrichment is dictated by the combination of the stellar mass-lifetime relation and the mass dependence of the yield, which should in principle differ from element to element. Other elements produced by slow neutron capture often have the highest yields from lower mass AGB stars. For example, Cristallo et al. (2011, 2015) report Sr yields that are dominated by $M_{\rm ZAMS} = 2-3\,{\rm M}_\odot$ progenitors (see Fig. 5 of Johnson & Weinberg 2020), giving it a characteristic delay time of ~ 500 Myr. The characteristic delay-times will be as long as a few Gyr if and only if the yields are dominated by $\lesssim 1.5\,{\rm M}_\odot$ stars.

In the right panel of Fig. 4, we plot the total amount of N produced by a 13.2 Gyr old single stellar population as a function of its initial metallicity according to all of our AGB star yield tables, including the linear model (see equation 3 and discussion in § 2.2). For this calculation, we include the metallicity independent CCSN yield ($y_N^{\rm CC} = 3.6 \times 10^{-4}$; see discussion in § 2.1). In general, there is good qualitative agreement between the C11+C15 and the V13 models, the only major difference being the normalization. The predictions with the linear model with $\xi = 3 \times 10^{-4}$ are nearly identical to the C11+C15 model, which is unsurprising given their similarity in Fig. 3. The value at which these N yields flatten off at low Z is reflective of our adopted value of $y_N^{\rm CC}$. Up to $\log_{10}(Z/Z_\odot) \approx -0.2$, the KL16+K18 yields predict a similar trend as C11+C15 and V13, also with a difference in normalization, but at solar and supersolar metallicities they predict much more metallicity-independent N yields than others. The K10 yields, on the other hand, do not agree with any of the other models, instead predicting N yields to *decrease* monotonically with increasing Z. These differences between the K10 and KL16+K18 models trace back to differences regarding the opacity and mass loss prescriptions (see discussion in § 2.2). Although the normalization depends on the SN yields of all elements, we demonstrate in § 4.2 that reproducing the [N/O]-[O/H] relation as observed requires N yields which scale roughly linearly with metallicity as in the C11+C15 and V13 models.

3 THE MULTI-ZONE CHEMICAL EVOLUTION MODEL

We use the fiducial model for the Milky Way published in Johnson et al. (2021), which runs using the VICE GCE code (see Appendix A; Johnson & Weinberg 2020; Griffith et al. 2021a). Multi-zone models allow simultaneous calculations of abundances for multiple Galactic regions, making them a more physical option than classical one-zone models for a system like the Milky Way. Furthermore, they can take into account stellar migration in a framework that is much less computationally expensive than hydrodynamical simulations, making them the ideal experiments for our purposes. We provide a brief summary of the model here, but a full breakdown can be found in § 2 of Johnson et al. (2021).

As in previous models for the Milky Way with similar motivations (e.g. Matteucci & Francois 1989; Schönrich & Binney 2009; Minchev et al. 2013, 2014, 2017; Sharma et al. 2021), this model parameterizes the Galaxy disc as a series of concentric rings. With a uniform width of $\delta R_{\rm gal} = 100$ pc, each ring is assigned its own star formation history (SFH), and with assumptions about outflows and the $\Sigma_{\rm gas} - \dot\Sigma_\star$ relation (see discussion below), VICE computes the implied amounts of gas and infall at each timestep automatically. Under the caveat that stellar populations can move and place some of their nucleosynthetic products in rings other than the one they were born in, each ring is otherwise described by a conventional one-zone GCE model. Allowing stars to enrich distributions of radii was a novel addition to this type of model, and Johnson et al. (2021) demonstrated that this has a significant impact on enrichment rates from delayed sources such as SNe Ia.

To drive stellar migration, the model makes use of star particles from a hydrodynamical simulation, for which Johnson et al. (2021) select the h277 galaxy from the Christensen et al. (2012) suite evolved with the N-body+SPH code GASOLINE (Wadsley et al. 2004); we retain this decision here. h277 spans 13.7 Gyr of evolution, but the sample of star particles with reliable birth radii span 13.2 Gyr in age; the model thus places the onset of star formation ~ 500 Myr after the big bang and integrates up to the present day. Previous studies have shown that h277, among other disc galaxies evolved with similar physics, has a realistic rotation curve (Governato et al. 2012; Christensen et al. 2014a,b), stellar mass (Munshi et al. 2013), metallicity (Christensen et al. 2016), dwarf satellite population (Zolotov et al. 2012; Brooks & Zolotov 2014), HI properties (Brooks et al. 2017), and stellar age-velocity relation (Bird et al. 2021). Despite this, there are some interesting differences between h277 and the Milky Way. First and foremost, h277 had only a weak and transient bar and lacks one at the present day, while the Milky Way is known to have a strong, long-lived central bar (e.g. Bovy et al. 2019). This could indicate that the dynamical history of h277 and its star particles differs significantly from that of the Milky Way. Furthermore, the last major merger in h277 was at a redshift of $z \approx 3$, making it an interesting case study for its quiescent merger history (e.g. Zolotov et al. 2012), while the Sagitarrius dwarf galaxy is believed to have made pericentric passages around the Milky Way at $1-2$ Gyr intervals (Law & Majewski 2010). With this in mind, a dynamical history such as that of h277 in this GCE model can be thought of as capturing purely secular galaxy evolution. Although these differences between h277 and the Milky Way are well understood, their impact on chemical evolution is not. We are unaware of any studies which investigate the impact of different assumptions regarding the Galaxy's dynamical history and the subsequent effects on predicted abundances; we plan to pursue this question in future work.

Radial migration of stars proceeds from the h277 star particles in a simple manner; for a stellar population in our model born at a radius $R_{\rm birth}$ and a time $T_{\rm birth}$, VICE searches for star particles born at $R_{\rm birth} \pm 250$ pc and $T_{\rm birth} \pm 250$ Myr. From the star particles that make this cut, it then randomly selects one to act as that stellar population's *analogue*. The stellar population then assumes the present day midplane distance z and the change in orbital radius $\Delta R_{\rm gal}$ of its analogue between its birth and the present day. In the Johnson et al. (2021) fiducial model, stellar populations move to their implied final radii with a $\sqrt{\rm age}$ dependence according to:

$$R_{\rm gal}(T) = R_{\rm birth} + \Delta R_{\rm gal} \sqrt{\frac{T - T_{\rm birth}}{13.2\,{\rm Gyr} - T_{\rm birth}}}, \qquad (4)$$

where 13.2 Gyr is simply the present day (see discussion above). With displacement proportional to $\sqrt{\rm age}$, this corresponds to a scenario in which radial migration proceeds as a diffusion process as modeled by Frankel et al. (2018, 2019) and supported by the N-body simulations of Brunetti, Chiappini & Pfenniger (2011). Although Johnson et al. (2021) investigated other assumptions for this time-dependence, in the present paper we only use this parameterization (hereafter referred to as the "diffusion" model) and an idealized one in which stars remain at their birth radius until they instantaneously migrate at the present day (hereafter referred to as the "post-processing" model). If VICE does not find any star particles from h277 in its initial $R_{\rm gal} \pm 250$ pc and $T \pm 250$ Myr search, it widens it to $R_{\rm gal} \pm 500$ pc

and $T \pm 500$ Myr; if still no candidate analogues are found, `VICE` maintains the $T \pm 500$ Myr requirement, but assigns the star particle with the smallest difference in birth radius as the analogue. This procedure can be thought of as "injecting" the dynamics of the `h277` galaxy into our multi-zone chemical evolution model, and can in principle be repeated for any hydrodynamical simulation of a disc galaxy. As in Johnson et al. (2021), we neglect radial gas flows (e.g. Lacey & Fall 1985; Bilitewski & Schönrich 2012; Vincenzo & Kobayashi 2020), instead focusing on the impact of stellar migration.

Rather than using a hydrodynamical simulation, some previous studies have implemented stellar migration using dynamical arguments (e.g. Schönrich & Binney 2009; Sharma et al. 2021). An advantage of our approach over this is that these dynamical arguments introduce free parameters which then require fitting to data. It is also unclear to what extent the fit might bias the model into agreement with quantities in the sample not involved in the fit. A disadvantage of our approach is that we are restricted to one realization of our dynamical history; slight variations are not possible. We do not distinguish between "blurring" and "churning", terms commonly used to refer to changes in the guiding centre radii of stars and their epicyclic motions, respectively. Both are induced by a variety of physical interactions such as molecular cloud scattering (Mihalas & Binney 1981; Jenkins & Binney 1990; Jenkins 1992), orbital resonances with spiral arms or bars (Sellwood & Binney 2002; Minchev et al. 2011), and satellite perturbations (Bird, Kazantzidis & Weinberg 2012). All of these effects are included in `h277` and should therefore be inherited by the stellar populations in our GCE model.

We assume the SFH of the "inside-out" model from Johnson et al. (2021). The time-dependence at a given $R_{\rm gal}$ is described by

$$\dot{\Sigma}_\star \propto (1 - e^{-t/\tau_{\rm rise}}) e^{-t/\tau_{\rm sfh}}, \quad (5)$$

where $\tau_{\rm rise}$ approximately controls the amount of time the SFR is rising at early times; we set this parameter equal to 2 Gyr at all radii as in Johnson et al. (2021). Our e-folding timescales of $\tau_{\rm sfh}$ are taken from a fit of this functional form to the $\Sigma_\star$-age relation in bins of $R/R_{\rm e}$ for $10^{10.5} - 10^{11}$ $M_\odot$ Sa/Sb Hubble type spiral galaxies reported by Sánchez (2020). The resulting values of $\tau_{\rm sfh}$ are long: ~15 Gyr at the solar circle ($R_{\rm gal}$ = 8 kpc) and as high as ~40 Gyr in the outer disc (see Fig. 3 of Johnson et al. 2021). This is a consequence of flat nature of the $\Sigma_\star$-age relation reported by Sánchez (2020).

Within each $\delta R_{\rm gal} = 100$ pc ring, the normalization of the SFH is set by the total stellar mass of the Milky Way disc and the present-day stellar surface density gradient, assuming that it is unaffected by migration (see Appendix B of Johnson et al. 2021). For the former, we neglect the contribution from the bulge and adopt the total disc stellar mass of 5.17×10^{10} $M_\odot$ from Licquia & Newman (2015). For the latter, we adopt a double exponential form describing the thin- and thick-disc components. We take the scale radii of the thin- and thick-discs to be $R_{\rm t}$ = 2.5 kpc and $R_{\rm T}$ = 2.0 kpc, respectively, with a surface density ratio at $R_{\rm gal} = 0$ of $\Sigma_{\rm T}/\Sigma_{\rm t} = 0.27$ based on the findings of Bland-Hawthorn & Gerhard (2016).

Since the Johnson et al. (2021) models run `VICE` with the SFH specified a priori, determining the gas supply requires an assumption regarding SFE. Based on the findings of Kennicutt (1998), GCE models often adopt a single power-law relating the surface density of gas $\Sigma_{\rm gas}$ to the surface density of star formation $\dot{\Sigma}_\star$. Recent studies, however, have revealed that the $\Sigma_{\rm gas} - \dot{\Sigma}_\star$ relation is much more nuanced on a galaxy-by-galaxy basis (de los Reyes & Kennicutt 2019; Ellison et al. 2021; Kennicutt & de los Reyes 2021). Some of the uncertainty regarding its details can be traced back to the ongoing

debate about the CO-to-H$_2$ conversion factor (Kennicutt & Evans 2012; Liu, Gao & Greve 2015). Based on a compilation of the Bigiel et al. (2010) and Leroy et al. (2013) data shown in comparison to the theoretically motivated parameterizations of Krumholz et al. (2018, see their Fig. 2), Johnson et al. (2021) take a three-component power-law $\dot{\Sigma}_\star \propto \Sigma_{\rm gas}^N$ with index N given by:

$$N = \begin{cases} 1.0 & (\Sigma_{\rm gas} \geq 2 \times 10^7 \text{ M}_\odot \text{ kpc}^{-2}) \\ 3.6 & (5 \times 10^6 \text{ M}_\odot \text{ kpc}^{-2} \leq \Sigma_{\rm gas} \leq 2 \times 10^7 \text{ M}_\odot \text{ kpc}^{-2}) \\ 1.7 & (\Sigma_{\rm gas} \leq 5 \times 10^6 \text{ M}_\odot \text{ kpc}^{-2}). \end{cases} \quad (6)$$

The normalization is set by letting the SFE timescale $\tau_\star \equiv \Sigma_{\rm gas}/\dot{\Sigma}_\star$ at surface densities where $N = 1$ be given by the value derived observationally for molecular gas, denoted by $\tau_{\rm mol}$. This value at the present day is taken to be $\tau_{\rm mol,0} = 2$ Gyr (Leroy et al. 2008, 2013) with a $t^{1/2}$ dependence on cosmic time based on the findings of Tacconi et al. (2018) studying the properties of molecular gas as a function of redshift.

With the yields adopted in the Johnson et al. (2021) models (see discussion at the beginning of § 2), considerable outflows are required in order to predict plausible abundances. Weinberg et al. (2017) demonstrate analytically that the equilibrium abundance of some element in the gas phase is approximately determined by its yield and the mass loading factor $\eta \equiv \dot{\Sigma}_{\rm out}/\dot{\Sigma}_\star$ with a small correction for the SFH. Johnson et al. (2021) select a scaling of η with $R_{\rm gal}$ such that the equilibrium abundance as a function of radius corresponds to a reasonable metallicity gradient within the Galaxy (see their Fig. 3 and discussion in their § 3.1). Nonetheless, yields and the strength of outflows are mutually degenerate parameters since they act as source and sink terms in computing enrichment rates. The absolute scale of nucleosynthetic yields is a topic of debate (see discussion in, e.g., Griffith et al. 2021a), and some authors even neglect outflows entirely, arguing that they do not significantly alter the chemical evolution of the Galaxy disc (e.g. Spitoni et al. 2019, 2021). We investigate the impact of simultaneous variations in our yields and the efficiency of outflows in § 4.2 below.

4 RESULTS

4.1 Evolution of a Fiducial Model

Our fiducial model adopts $y_{\rm N}^{\rm CC} = 3.6 \times 10^{-4}$ and our linear AGB star yield model with $\xi = 9 \times 10^{-4}$ (see equation 3) along with the O and Fe yields of Johnson et al. (2021, see discussion in § 2.1). Although we presented this model in comparison to the C11+C15 yields with $\xi = 3 \times 10^{-4}$ in Fig. 3, we find that a renormalization of this model is necessary to reproduce the [N/O]-[O/H] relation as observed; we discuss this point further in § 4.2. To demonstrate the impact of stellar migration on N enrichment rates, we make use of the diffusion migration model in this section (see discussion in § 3).

In the left panel of Fig. 5, we plot the evolution of N and O abundances in the gas phase at five different Galactocentric radii. At early times, [O/H] is low and [N/O] reflects the ratio of the CCSN yields ([N/O]$_{\rm cc} \approx -0.7$). Consequently, the tracks in each ring are similar. Once lower mass stars begin to evolve through an AGB phase, they enrich the interstellar medium (ISM) with N but negligible amounts of O, increasing [N/O]. At this point, the tracks in each ring separate from one another. This separation is a consequence of the metallicity gradient in [O/H] being established early in the Galaxy's evolution. The radial gradient in our model arises out of a decrease in the equilibrium abundance of O with increasing radius. Produced on short
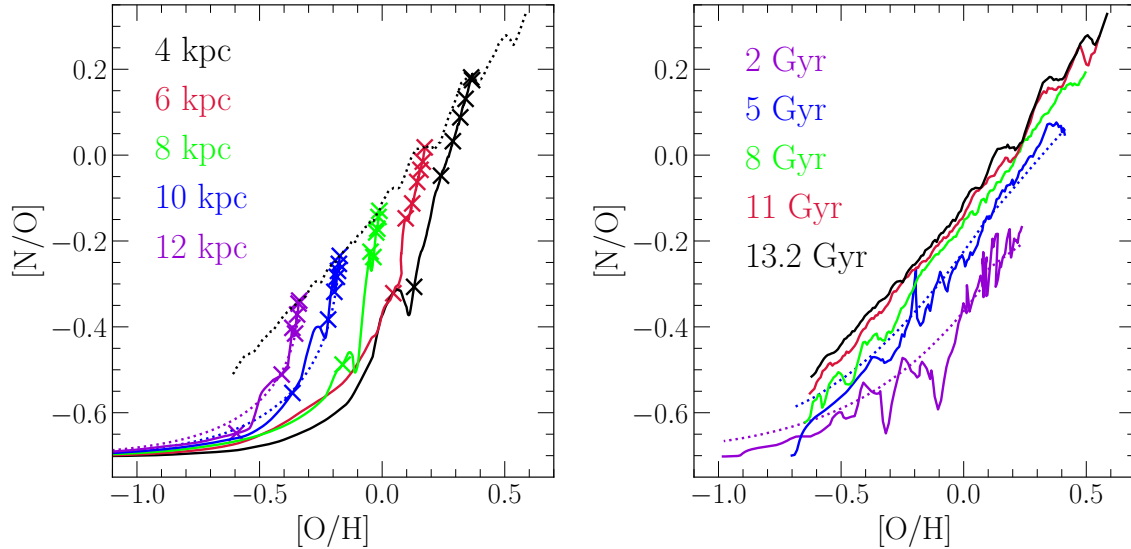
Figure 5. **Left**: The gas-phase [N/O]-[O/H] relation parameterized by time at fixed radius (solid coloured lines) in the fiducial model. X's denote the abundances at T = 2, 4, 6, 8, 10, 12, and 13.2 Gyr (the present day) at all radii. The dotted black line is the same as the solid black line in the right panel. Coloured dotted lines mark the evolution of our model at R_{gal} = 10 and 12 kpc when we neglect the impact of stellar migration on enrichment rates (i.e. the "post-processing" migration model from Johnson et al. 2021; see discussion in § 3). **Right**: The gas-phase [N/O]-[O/H] relation parameterized by radius at various snapshots (solid coloured lines) in our fiducial model. Similar to the left panel, coloured dotted lines denote the resulting relation at T = 2 and 5 Gyr when we neglect stellar migration in computing enrichment rates.

timescales by CCSNe, O achieves equilibrium faster than elements produced by delayed nucleosynthetic sources (Weinberg et al. 2017). The ISM therefore reaches equilibrium in O soon after AGB stars begin producing N, after which [N/O] continues to increase at an approximately fixed [O/H] at all radii (see also Fig. 8 and associated discussion in § 4.4). The separation of these evolutionary tracks contests the popular interpretation that the [N/O]-[O/H] relation arises as an evolutionary sequence, instead suggesting a superposition of endpoints. Similar arguments have been made regarding low [α/Fe] disc stars (e.g. Schönrich & Binney 2009; Nidever et al. 2014; Buck 2020; Sharma et al. 2021). In short, a given ring in our model does not evolve along the [N/O]-[O/H] relation, instead following this "rightward-then-upward" trajectory dictated by the timescales on which N and O achieve equilibrium.

Because there is a delay between a stellar population's formation and N production from its AGB stars (~250 Myr in this model; see Fig. 4), stellar migration can in principle occur within this time interval. Although the bulk of migration occurs on longer timescales, this characteristic delay is comparable to the dynamical time of the Milky Way and is thus adequate for kinematic heating to at least begin. In zoom-in hydrodynamical simulations from the FIRE[1] suite (Hopkins et al. 2014), El-Badry et al. (2016) indeed find that stars in a $M_\star \approx 10^{10.6}$ $M_\odot$ galaxy can migrate $1 - 2$ kpc within 1 Gyr of their formation. Consequently, N enrichment rates at fixed R_{gal} may differ significantly from their expected values given the SFH at that radius because stellar migration induced a deficit or surplus of N-producing AGB stars. These tracks can thus move vertically in the [N/O]-[O/H] plane in response to AGB stars moving between rings as the Galaxy evolves. We demonstrate this effect by comparing the solid blue and purple lines to their dotted counterparts. These are the tracks we compute using the post-processing migration model which

neglects the impact of migration on enrichment rates (see discussion in § 3).

In the right panel of Fig. 5, we plot the gas-phase [N/O]-[O/H] relation predicted by the model at various snapshots. To obtain this, we simply take the N and O abundances in the ISM at a given output time for each δR_{gal} = 100 pc ring at R_{gal} > 2 kpc and plot them as a line. The relation is generally time-independent at $T \gtrsim 5$ Gyr. Although there is some slight evolution toward higher [N/O], the total change in [N/O] over this time interval is well within the intrinsic scatter derived observationally (see Fig. 1). Even at T = 2 Gyr at a redshift of $z \approx 2.6$ (when the universe was 2.5 Gyr old, see discussion in § 3), [N/O] at fixed [O/H] is only ~0.2 dex lower than its value at the present day. Especially when considering the intrinsic scatter that would arise if we were to consider models with, e.g., different SFHs, this supports previous arguments that the redshift evolution of the [N/O]-[O/H] relation is at most minimal (Vincenzo & Kobayashi 2018; Hayden-Pawson et al. 2021).

We again demonstrate the impact of stellar migration in the right panel of Fig. 6 by comparing the blue and purple solid lines to their dotted counterparts, which quantify the relation using the post-processing migration model. This indicates that the complex features seen in the relation at all times are a consequence of migration as discussed above. The mechanism by which stellar migration imposes these features in the [N/O]-[O/H] plane is qualitatively similar to what Johnson et al. (2021) find for SN Ia production of Fe (see discussion in their §§ 3.1 and 3.4). They found that the SN Ia rate in this model can vary by as much as a factor of ~3 at large radii ($R_{gal} \gtrsim 9$ kpc). When a deficit or surplus of SN Ia events is sustained for timescales comparable to the depletion time of the local ISM, the gas-phase abundance of Fe increases or decreases accordingly. As a consequence, some of the stellar populations that form during these events are Fe-poor enough to present as young stars ($\lesssim 6$ Gyr) with significantly super-solar [α/Fe] ratios. Stars with these ages and chemical compositions have indeed been observed in the solar neigh-

---

[1] https://fire.northwestern.edu
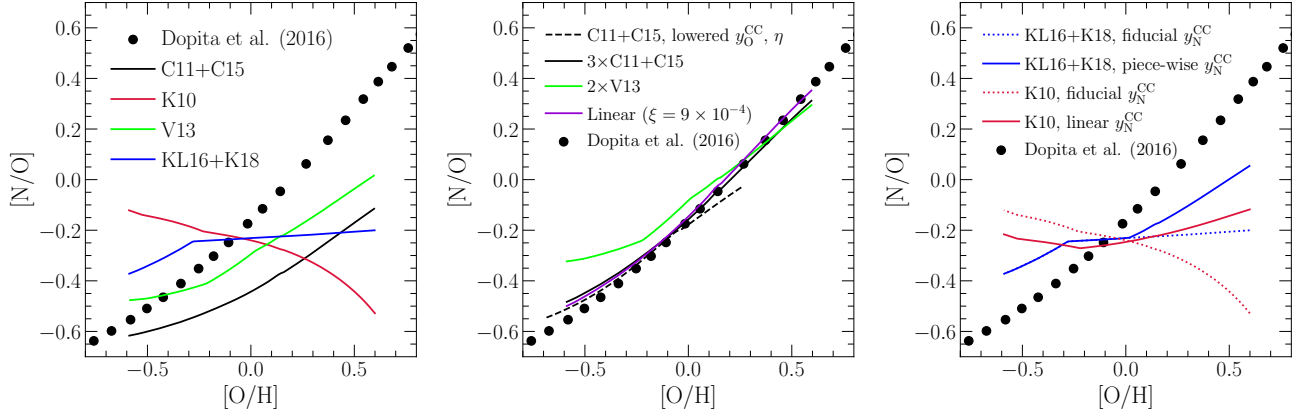
Figure 6. Left: The present-day gas-phase [N/O]-[O/H] relation predicted by our model with each of the four AGB star yield tables predict by stellar evolution models discussed in § 2.2, colour-coded according to the legend. We include the Dopita et al. (2016) measurements of this relation for local stars and HII regions (duplicated from Fig. 1) as the observational benchmark. **Middle**: The same as the left panel, but for a case where we artificially amplify the C11+C15 yields by a factor of 3 and the V13 yields by a factor of 2. We show our fiducial model using the linear AGB star yields with a slope of $\xi = 9 \times 10^{-4}$ in a solid purple line. The black dashed line quantifies a model in which the C11+C15 yields are unmodified, but SN yields and the outflow mass loading factor are lowered by a factor of 3 (see discussion in § 4.2.1). **Right**: The same as the left panel, but comparing the predictions made by the K10 and KL16+K18 yields with our fiducial value of y_N^{CC} (dotted lines, same as left-hand panel) to those with alternate forms of y_N^{CC} (solid lines; see equations 7 and 8 and discussion in § 4.2). We show all predictions with our post-processing migration model (see discussion in § 3).

bourhood with APOGEE (Chiappini et al. 2015; Martig et al. 2015, 2016; Warfield et al. 2021). Although a substantial portion of the observed stars appear to have undergone mass transfer from a binary companion, allowing them to masquerade as younger objects (Jofré et al. 2016; Yong et al. 2016; Izzard et al. 2018; Silva Aguirre et al. 2018; Miglio et al. 2021), some exhibit [C/N] ratios consistent with truly young ages (Hekker & Johnson 2019). Johnson et al. (2021) argue that the impact of stellar migration on enrichment rates is responsible for this intrinsically young sub-component (see discussion in their § 3.4). In the case of N, the effect is much smaller ($\lesssim 0.1$ dex in [N/O]), but Fig. 5 suggests there are some instances at early times where the effect is more substantial. This arises because our model predicts N yields to be ejected from stellar populations ~5 times faster than Fe (even faster in our alternate yield models with larger contributions from high mass AGB stars; see Fig. 4 and discussion in § 2.3). Consequently, there is much less time for stellar migration to occur within the timescale of N production than there is within the timescale of Fe production. This underscores the argument from Johnson et al. (2021) that the impact of stellar migration on enrichment rates is more substantial for elements produced on longer characteristic delay times.

4.2 Comparison to Observed Gas-Phase Trends

We use the Dopita et al. (2016) measurements as our observational benchmark. They are a good representation of many results for gas-phase N and O abundances (see Fig. 1), and they agree well with APOGEE stellar trends (Vincenzo et al. 2021). To make the comparison between different yield models more clear, we neglect the impact of stellar migration on enrichment rates and make use of the post-processing migration model in this section (see discussion in § 3).

In the left panel of Fig. 6, we compare our model predictions with each of the AGB star yield tables predicted from stellar evolution models (see Fig. 3 and discussion in § 2.2). With no changes to the Johnson et al. (2021) parameterization of the model, all

four AGB star yield tables fail to reproduce the [N/O]-[O/H] relation as observed. The C11+C15 and V13 yields are able to reproduce the qualitative trend, but with an incorrect normalization. The K10 and KL16+K18 yields, on the other hand, fail to reproduce the steadily sloped increase of [N/O] with [O/H]. The inverse dependence of [N/O] with [O/H] predicted by the K10 AGB star yields can be understood by the interaction between TDU and HBB (see discussion in § 2.2). Both effects are stronger at low metallicity, and since all of the K10 stars experiencing HBB also experience TDU (see their Table 1), such a result is unsurprising. This is also true for the KL16+K18 yields, but that model predicts a relatively flat [N/O]-[O/H] relation because of updated model inputs regarding opacity and mass loss and the impact this has on ^{14}N yields (see discussion in § 2.2).

4.2.1 Simultaneous Variations in Outflows and SN Yields

In order to successfully reproduce the observations with the C11+C15 and V13 yields, we find that we must artificially amplify them by factors of ~3 and ~2, respectively. We illustrate the results of these modified yield models and for our fiducial linear model with a slope of $\xi = 9 \times 10^{-4}$ in the middle panel of Fig. 6. Although the V13 model predicts an [N/O]-[O/H] relation that is slightly shallower than the Dopita et al. (2016) measurements, the predictions are reasonably within the scatter seen in Fig. 1. Rather than artificially amplifying the C11+C15 and V13 yields, we also find good agreement with the observed relation if we lower both our SN yields and our outflow mass loading factor η as a function of R_{gal} by similar factors from their values in Johnson et al. (2021). These parameters, which approximately determine the equilibrium abundance in a one-zone model (Weinberg et al. 2017), are tuned to reproduce a metallicity gradient in the disc that resembles that observed for the Milky Way (see discussion in § 2.4 of Johnson et al. 2021). However, since the yield and the outflow are simply source and sink terms in computing enrichment rates, the model makes similar predictions when both are raised or lowered by the same factor. We demonstrate this point in the middle panel of Fig. 6 with the black

dashed line for the unmodified C11+C15 yields with both y_O^{CC} and η each lowered by a factor of 3. This model spans a different range in [O/H] because the relation between y_O^{CC}, η, and the equilibrium abundance is only approximately one-to-one, but the predictions also exhibit good agreement with the Dopita et al. (2016) measurements.

Lowering our SN yields by a factor of $2 - 3$ is plausible if a substantial fraction of massive stars collapse directly to black holes as opposed to exploding as SNe at the ends of their lives. Our IMF-averaged massive star yields (see discussion in §2.1) are based on a Kroupa (2001) IMF combined with SN nucleosynthesis models in which most $M > 8$ M$_\odot$ stars explode as a CCSN (e.g. Woosley & Weaver 1995; Chieffi & Limongi 2004, 2013; Limongi & Chieffi 2018; Nomoto et al. 2013), but recent results contest the validity of this assumption. The criteria for massive star explosions and which stars of what masses end their lives in "failed supernovae" has been a recent topic of interest from both theoretical (e.g. Pejcha & Thompson 2015; Sukhbold et al. 2016; Ertl et al. 2016) and observational perspectives (e.g. Gerke, Kochanek & Stanek 2015; Adams et al. 2017; Basinger et al. 2021). Although there is presently no combination of a SN nucleosynthesis model with a physically motivated black hole landscape that is able to reproduce the observed abundance patterns (Griffith et al. 2021a), black hole formation still lowers SN yields by simply not ejecting massive star envelopes to the ISM. With VICE's vice.yields.ccsne.fractional function, designed to calculate values of y_X^{CC} for various elements (see discussion in § 2.1 here and in § 4 of Griffith et al. 2021a), we indeed find a value of $y_O^{CC} = 0.0056$ using the W18 explosion model from Sukhbold et al. (2016) compared to our fiducial value of $y_O^{CC} = 0.015$. Through this mechanism relating N yields to the CCSN yields of O via [N/O] ratios and consequently to the black hole landscape, the C11+C15 and V13 models favor a scenario in which a substantial fraction of massive stars produce failed supernovae, significantly suppressing O yields by a factor of $2 - 3$. If instead most massive stars successfully explode as CCSNe, these AGB star yields must increase by a similar factor to offset the additional O yield under the more explosive black hole landscape.

Alternatively, Vincenzo et al. (2016a) are able to reproduce the [N/O]-[O/H] relation in chemical evolution models with the V13 yields by implementing a differential wind in which outflows remove O but not N from the star forming gas reservoir. Because the enrichment rates are the same as in our models with lowered yields, we find similar results if we simply add a portion of the SN products (both CCSN and SN Ia) directly to the outflow while still lowering η at all radii. If SNe are the sources of outflow-driving winds but AGB stars do not significantly contribute, it would be reasonable to expect some portion of the SN ejecta to be swept up by the wind; recent theoretical (Christensen et al. 2018) and observational arguments (Chisholm, Tremonti & Leitherer 2018) indeed suggest such a scenario.

4.2.2 Metallicity-Dependent CCSN Yields of N

With the K10 and KL16+K18 models failing to explain the qualitative trend of [N/O] with [O/H], none of the variations discussed in § 4.2.1 in the context of the C11+C15 and V13 yields are able to repair their predictions. Each of these alternate parameterizations corresponds to a renormalization of the predicted [N/O]-[O/H] relation, and with inaccurate slopes, there is no factor by which the predicted [N/O] ratios can be amplified or diminished in order to accurately explain the data. However, in principle it is possible that a metallicity-dependent CCSN yield of N could make up the difference.

In order for the KL16+K18 yields to reproduce the observations, N abundances at high [O/H] must increase. The non-rotating CCSN models of Nomoto et al. (2013) suggest that y_N^{CC} may increase at super-solar metallicity (see Fig. 2). Perhaps this could make up the difference. We therefore construct the following parameterization of y_N^{CC} for use with the KL16+K18 AGB star yields:

$$y_N^{CC} = (3.6 \times 10^{-4}) \max\left(1, \frac{Z}{Z_\odot}\right). \tag{7}$$

This yield maintains our baseline value of $y_N^{CC} = 3.6 \times 10^{-4}$ at sub-solar metallicities motivated by the rotating models of Limongi & Chieffi (2018) but adds a significant secondary yield component at higher Z as suggested by non-rotating models. In order for the K10 yields to successfully reproduce the observations, the sign of the [N/O]-[O/H] relation must flip: the N abundances at high (low) Z must increase (decrease). In a similar fashion, we construct the following parameterization of y_N^{CC} for use with the K10 AGB star yields:

$$y_N^{CC} = (3.6 \times 10^{-4})\left(\frac{Z}{Z_\odot}\right) \tag{8}$$

This yield is motivated by the non-rotating CCSN models quantified in Fig. 2, in which we also illustrate these parameterizations with the slanted black dotted line. Although this model with y_N^{CC} given by equation (8) and the K10 AGB star yields does not include a primary component in that the AGB star and CCSN yields both depend on metallicity, the combination is qualitatively motivated by reproducing the [N/O]-[O/H] relation as observed.

We compare our GCE model predictions with these alternate yield parameterizations for the K10 and KL16+K18 AGB star yield models in the right-hand panel of Fig. 6. These metallicity-dependent CCSN yields are able to make up some of the difference, but both models still predict an [N/O]-[O/H] relation that is simply too shallow to explain the observations. In principle, there are parameterizations of y_N^{CC} which could reproduce the [N/O]-[O/H] relation with the K10 and KL16+K18 yield models - whatever makes up the difference at a given [O/H] can be assumed to be the corresponding CCSN yield. Such assumptions, however, would be challenged by both the rotating and non-rotating SN nucleosynthesis models illustrated in Fig. 2. Despite these results, we cannot say with any confidence whether or not such a wide mass range of stars should experience both TDU and HBB during the AGB phase as in K10 and KL16+K18. Although this makes it difficult for these models to predict a monotonic increase of [N/O] with [O/H] because both processes are more efficient at low metallicity (see discussion in § 2.2), there are many uncertain parameters required to predict yields from stellar evolution models, and each of the previously published tables we have investigated capture only a handful of realizations of them.

In short, we find that in order to reproduce the gas-phase [N/O]-[O/H] relation as observed, our model requires the metallicity dependence characteristic of the secondary N yield to be approximately linear with Z. We find in general that describing the primary component as a metallicity-independent CCSN yield and the secondary component as a metallicity-dependent AGB star yield is a simple recipe that our GCE models have sufficient success with. We have previously illustrated this dependence in the right panel of Fig. 4 for our fiducial model - the linear AGB star yield with slope $\xi = 9 \times 10^{-4}$ and $y_N^{CC} = 3.6 \times 10^{-4}$. These yields are appropriate for GCE models with strong outflows and massive star yields suggested by models in which most M > 8 M$_\odot$ stars explode as a CCSN. In models with weaker outflows and lower massive star yields due to extensive black
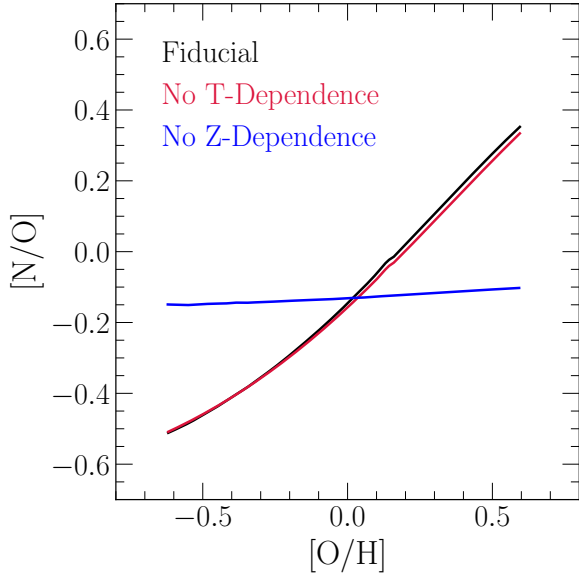
Figure 7. A comparison between our fiducial model with post-processing migration (black) and variations with the time dependence (red) and metallicity dependence removed (blue). To remove the time dependence, we pre-compute the AGB star yields of N from 13.2 Gyr old stellar populations as a function of metallicity as in the right panel of Fig. 4, then incorporate this into the prompt CCSN yields and set the delayed AGB star contribution to zero. To remove the metallicity dependence, we evaluate the yields at our assumed solar metallicity of $Z = 0.014$ at all timesteps.

hole formation, the N yields may be up to ~3 times smaller. Indeed the unmodified C11+C15 yields follow a slope of $\xi = 3 \times 10^{-4}$ quite closely as we have demonstrated in Fig. 3.

4.3 The Importance of the Metallicity Dependence of the Yield

Despite predicting a different mass dependence for y_N^{AGB} (see Fig. 3), the renormalized C11+C15 and V13 yield models both reproduce the slope of the [N/O]-[O/H] relation reasonably well. This is an indication that perhaps the metallicity dependence plays a much more important role than the DTD in establishing this correlation. To investigate this further, we consider two variants of our fiducial model: one with the dependence on stellar age (or, equivalently, stellar mass) removed from the enrichment rate calculations, and the other with the metallicity dependence removed. To make this comparison more straightforward, we use the post-processing migration model (see discussion in § 3).

To remove the age dependence, we simply eject the AGB star yields alongside the CCSN yield instantaneously after a single stellar population forms. We pre-compute the N yields from all AGB stars associated with a 13.2 Gyr old stellar population as a function of progenitor metallicity in a similar fashion as in the right panel of Fig. 4; we use the linear yield model with slope $\xi = 9 \times 10^{-4}$ in this section. Since VICE works from IMF-averaged CCSN yields assumed to be injected instantaneously following a single stellar population's formation (see discussion in § 2.1), we make use of the software's capability to let the user specify functional forms for nucleosynthetic yields and simply add this N yield to y_N^{CC} and set y_N^{AGB} to zero. In this model, y_N^{CC} inherits a metallicity dependence from the AGB star yields and has the exact shape of the purple curve in the right hand panel of Fig. 4. To remove the metallicity dependence, the

procedure is much simpler: we simply evaluate y_N^{AGB} at our assumed solar metallicity of $Z = 0.014$ at all timesteps regardless of that which is predicted for a stellar population. In this variation, AGB star production still occurs on a DTD inherited from the stellar mass-lifetime relation and the mass dependence of the linear yield model.

We illustrate these model predictions in Fig. 7. The model with no age dependence is nearly identical to the [N/O]-[O/H] relation found in our fiducial model, while the model with no metallicity dependence is considerably different. This indicates that the metallicity dependence indeed plays a much larger role than the DTD in establishing the overall shape of the [N/O]-[O/H] relation. This is rather unsurprising given the short characteristic timescales of N production (~250 Myr, see the middle panel of Fig. 4). Mathematically, there is little difference in the enrichment rates if all of a stellar population's N is produced immediately as opposed to from a prompt, sharply declining DTD. The metallicity dependence, however, is paramount to the [N/O]-[O/H] relation, which is expected given the results in Fig. 3 and consistent with previous arguments that the increase in [N/O] at high [O/H] is a consequence of secondary N production (Vila-Costas & Edmunds 1993; van Zee et al. 1998; Henry & Worthey 1999; Pérez-Montero & Contini 2009; Berg et al. 2012; Pilyugin et al. 2012; Andrews & Martini 2013; Hayden-Pawson et al. 2021). This however does indicate that our GCE model offers little if any constraining power over the mass dependence of the AGB star yield of N.

4.4 Comparison to Stellar Abundances in the Milky Way Disc

Although N abundances are typically measured in the gas-phase in external galaxies, stellar abundances for the Milky Way are available through APOGEE (Majewski et al. 2017). By additionally making use of these data, we can investigate trends with stellar age and [O/Fe] at fixed metallicity. Before comparing the predictions of GCE models to N abundances derived from spectra of red giant samples such as APOGEE, it is essential to adjust the measurements for internal processes known to alter the surface compositions of stars because GCE models predict the birth abundances. During the main sequence lifetime of $M \gtrsim 1.3\ M_\odot$ stars, the CNO cycle processes much of the C and O nuclei in the core into ^{14}N. When the star evolves off the main sequence, this N-rich material is mixed with the outer convective layers, increasing the N abundance in the photosphere (Gilroy 1989; Korn et al. 2007; Lind et al. 2008; Souto et al. 2018, 2019). Using MESA stellar evolution models (Paxton et al. 2011, 2013, 2015, 2018) with standard mixing prescriptions, Vincenzo et al. (2021) developed a recipe to approximate the birth abundances of C, N and O and applied it to a sample of APOGEE/Kepler red giants with asteroseismic mass measurements. They found good agreement between the APOGEE abundances and the Dopita et al. (2016) measurements, and with our fiducial model's successful reproduction of their data, this indicates that it should also reproduce the [N/O]-[O/H] relation for APOGEE disc stars.

We find that our models predict a correlation between N and Fe abundances in the gas-phase which turns out to be important to understanding how the model predictions compare to stellar abundances. In Fig. 8, we plot the evolution of [N/H], [O/H], and [Fe/H] in the ISM at $R_{gal} = 4$, 8, and 12 kpc in our fiducial model with diffusion migration (see discussion in § 3). [N/H] is more correlated with [Fe/H] than [O/H] at all radii, and the relation persists up to lookback times of ~10 Gyr. This arises in part because N and Fe are both produced in significant quantities by delayed enrichment sources while O is produced almost entirely on short timescales by
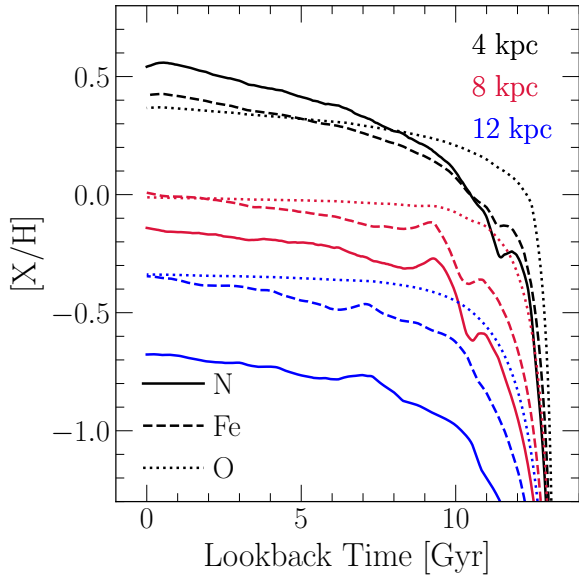
Figure 8. [N/H] (solid), [Fe/H] (dashed), and [O/H] (dotted) in the gas-phase as a function of lookback time in the fiducial model at $R_{\rm gal}$ = 4 (black), 8 (red), and 12 kpc (blue).

CCSNe (see discussion in § 2). Although the production timescale of N from single stellar populations is short (see discussion in § 2.3), metallicity dependent yields require more abundant species such as O to be produced and reach an equilibrium before N yields stabilize. When many stellar populations are present, the bulk of the N production will thus always follow the bulk production of more abundant species; this is qualitatively similar to what Johnson & Weinberg (2020) found regarding the production timescales of Sr and Fe. As a consequence of both its slight delay and its metallicity-dependent yields, N reaches its equilibrium abundance on timescales similar to Fe rather than O (Weinberg et al. 2017). Due to the prompt and metallicity independent nature of O enrichment, [O/H] is near equilibrium as far back as ∼10 Gyr ago while [N/H] and [Fe/H] are not.

Combining the Vincenzo et al. (2021) [N/O] ratios with the APOGEE stellar ages taken from Miglio et al. (2021), we illustrate the [N/O]-age relation in bins of [Fe/H] as predicted by our model in the left panel of Fig. 9. In good agreement with the observational measurements, the model predicts the [N/O]-age relation to be relatively flat in bins of [Fe/H]. This arises as a consequence of the N-Fe correlation and the fast approach to equilibrium in [O/H] as discussed above (see Fig. 8). A bin in [Fe/H] approximately corresponds to a bin in [N/H], and by extension a bin in [N/O] as well since [O/H] is nearly constant up to ∼10 Gyr ago. With uncorrected N abundances, Vincenzo et al. (2021) demonstrate that the [N/O]-age relation exhibits a significant negative slope at fixed [Fe/H] (see their Fig. 7), indicating that we would have erroneously found a tension between our model and the observations if we had used uncorrected measurements.

In the right panel of Fig. 9, we compare our model predictions to the [N/O]-[O/Fe] relation at fixed [O/H] reported by Vincenzo et al. (2021). The model correctly predicts a significant inverse relationship between [N/O] and [O/Fe]. This is again a consequence of the N-Fe correlation demonstrated in Fig. 8: [N/H] increases with [Fe/H], so at fixed [O/H], [N/O] increases as [O/Fe] decreases. This is another important success of our model; Vincenzo et al. (2021) demonstrate that even when stellar N abundances are corrected for internal mix-

ing processes, the chemical dichotomy in [N/O] between the high [α/Fe] and low [α/Fe] disc populations persists (for discussion of the Galaxy's two distinct chemical populations see, e.g., Hayden et al. 2015; Weinberg et al. 2019, 2021; Griffith et al. 2021b). Although the Johnson et al. (2021) model does not reproduce the [α/Fe] bimodality in detail (see discussion in their § 3.3), a future iteration which does should also reproduce it for [N/O] based on these results.

Quantitatively, our model slightly overpredicts [N/O] in the lower metallicity bins in both panels of Fig. 9. In general, our model occupies a noticeably wider range in [N/O] than do the Vincenzo et al. (2021) measurements at all ages and all [O/Fe]. This could be a sign that the AGB star yields of N in our fiducial model scale slightly too strongly with the total metallicity Z. Since our fiducial model assumes an exactly linear scaling of the N yield with Z (see equation 3), this suggests that perhaps a slightly sub-linear scaling would be more accurate, but only barely because the discrepancies in Fig. 9 are at the ∼0.1 dex level.

Although we demonstrate in § 4.3 that the metallicity dependence of the yield plays the strongest role in establishing the [N/O]-[O/H] relation, the DTD plays an important role in shaping the stellar abundances. In the model in which AGB nucleosynthetic yields are injected instantaneously along with CCSN products, the N-Fe correlation described above is no longer present. Instead, N approaches equilibrium on much faster timescales, resulting in it being much more correlated with O than Fe, and the resulting [N/O]-age relation is positively sloped at fixed [Fe/H]. This suggests that the DTD may play a minimal role in establishing gas-phase abundances but are important in shaping stellar abundances.

4.5 The Sources of Scatter in the [N/O]-[O/H] Relation

Schaefer et al. (2020) demonstrate that intrinsic scatter in the gas-phase [N/O]-[O/H] relation is correlated with variations in the local SFE. This is expected from one-zone GCE models (e.g. Mollá et al. 2006; Vincenzo et al. 2016a). However, Schaefer et al. (2020) did not rule out radial migration as another potential source of scatter in this relation. Although we have demonstrated in § 4.1 that the impact of stellar migration on enrichment rates is small, it could nonetheless contribute significantly to scatter in the observed [N/O]-[O/H] relation. Our models, taking into account the effects of migration on the enrichment rates while allowing full control over the SFH and the SFE through VICE, are an ideal tool with which to address this question.

To this end, we construct two variants of our fiducial model. While the fiducial model specifies the SFH *a priori* and lets VICE compute the infall history $\dot{\Sigma}_{\rm in}$, here we specify the infall history as a function of radius and time. As we will demonstrate below, the effects of dilution play an important role in driving variations in the [N/O]-[O/H] plane in these variants, and by specifying the infall history we have more control over the amount of dilution. In a similar fashion as in our fiducial model, we normalize $\dot{\Sigma}_{\rm in}$ such that a stellar mass consistent with that reported by Licquia & Newman (2015) arises from the simulation. All other evolutionary parameters are the same as in the Johnson et al. (2021) fiducial model (see discussion in § 3 for details).

In the first variant, the SFE exhibits 50% sinusoidal oscillations with time over 2 Gyr periods:

$$\tau_\star(R_{\rm gal}, t) = \tau_{\star,\rm J21}(R_{\rm gal}, t)\left(1 + 0.5\sin\left(\frac{2\pi t}{2\,{\rm Gyr}}\right)\right). \tag{9}$$

The infall rate is constant in each ring with a value determined
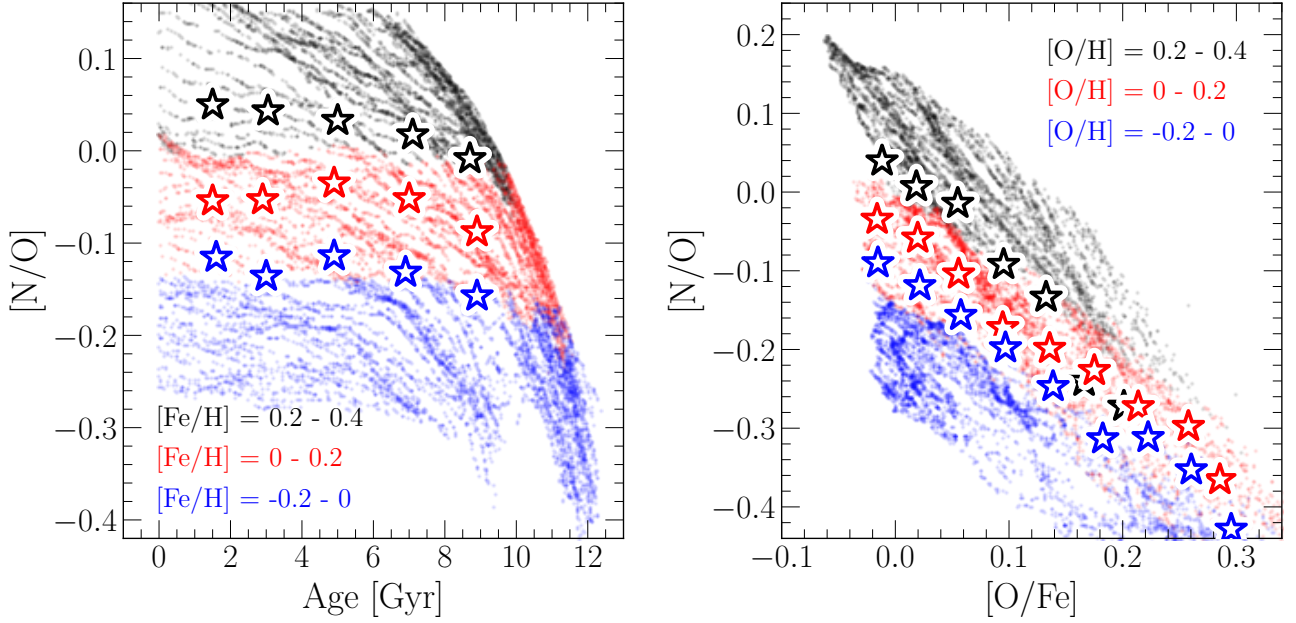
Figure 9. **Left**: [N/O] as a function of stellar age for 5000 stars randomly sampled from our model stellar populations in three bins of [Fe/H] (coloured points). Stars quantify the median trend in [N/O] with age using N abundances corrected for internal mixing processes reported by Vincenzo et al. (2021) in the same bins of [Fe/H]. **Right**: The same as the left panel, but instead showing [N/O] as a function of [O/Fe] in bins of [O/H].

by normalizing to the present day stellar mass and stellar surface density gradient of the Milky Way. Our choice of a 50% amplitude is comparable to the observationally derived scatter in molecular gas depletion times according to multiple measurement methods (see Figs. 4 and 5 of Tacconi et al. 2018 and references therein). Furthermore, variations in the SFE are of similar magnitude in h277, the galaxy from which our model's migration history is drawn. In the second variant, the SFE is constant and the infall rate oscillates with a 75% amplitude about its value in the first variant:

$$\dot{\Sigma}_{\rm in}(R_{\rm gal}, t) = \langle \dot{\Sigma}_{\rm in} \rangle \left(1 + 0.75 \sin \left(\frac{2\pi t}{2\,{\rm Gyr}} \right) \right). \quad (10)$$

The amplitude of 75% is chosen such that the ensuing variability in the SFR is of similar magnitude between the two models (~40%). We additionally run a model in which neither the accretion rate nor the SFE oscillate, replacing the fiducial model used in previous sections with this constant infall model. Otherwise, the evolutionary differences beyond simple oscillations complicate the comparison.

These variant models characterize evolutionary pathways in which star formation is more episodic than previously explored. In a real galaxy, variability in the SFE and the SFR is likely non-sinusoidal and not with constant amplitude. A sample of galaxies will have different amplitudes and be seen at different phases in their variability, and the impact of this on their N and O abundances will present as intrinsic scatter in a sufficiently large sample. By comparing models with and without reasonable amounts of variability in these quantities while taking into account radial migration, we can nonetheless assess which quantities impact abundances more strongly and are thus the more likely causes of intrinsic scatter in the observed [N/O]-[O/H] relation.

In the left panel of Fig. 10, we plot the predicted gas-phase [N/O]-[O/H] relation for five snapshots covering one cycle of fluctuations induced by variability in $\tau_\star$ according to equation (9). This model predicts a ~0.1 dex dynamic range in [N/O] at fixed [O/H], whereas the constant model with no variability in $\tau_\star$ predicts the relation to be

quite steady over this time interval. This suggests that stellar migration, present in both the constant model and this oscillatory variant, does not induce significant variability in the [N/O]-[O/H] plane; however, we demonstrate below that its effects are nonetheless non-negligible. The minimal impact of stellar migration traces back to the timescales of N production from single stellar populations (see Fig. 4 and discussion in § 2.3): with most N production occurring within ~250 Myr of a stellar population's formation, most stars will not migrate far from their birth radius by the time they produce most of their N, and the resulting impact on abundances is small.

The behavior in the [N/O]-[O/H] plane predicted by the oscillatory SFE variant is driven by the constant tug-of-war between dilution and re-enrichment associated with oscillations in $\tau_\star$. When star formation quickens, O production increases in proportion. The ISM abundance and consequently the N yields increase as well. Because of the slight but nonetheless finite delay-time of its production by AGB stars, the N enrichment rate lags slightly behind O. [N/O] therefore decreases, and the ISM moves down and to the right in the [N/O]-[O/H] plane. When star formation eventually slows, O production again follows suit. The N enrichment rate, as before, lags slightly behind, and [N/O] increases; the ISM therefore moves up and to the left in the [N/O]-[O/H] plane. The result is an anti-clockwise loop, which we illustrate for the solar circle with a black dashed line in the left panel of Fig. 10. The effect is generally larger in [O/H] than in [N/O] (~0.1 dex versus ~0.05 dex in this example) because dilution affects both [O/H] and [N/H] similarly. In the model with oscillations in $\dot{\Sigma}_{\rm in}$, we find that qualitatively similar processes drive the evolution in abundances, but there are interesting differences in detail which we discuss below in the context of scatter in the observed trend.

In the middle and right panels of Fig. 10, we plot the scatter in the gas-phase [N/O]-[O/H] relation inferred observationally by Schaefer et al. (2020). Using data from the MaNGA IFU survey (Bundy et al. 2015), they measure N and O abundances in 709,541 spaxels across 6,507 unique galaxies spanning $10^9 - 10^{11}$ M$_\odot$ in stellar mass. Since
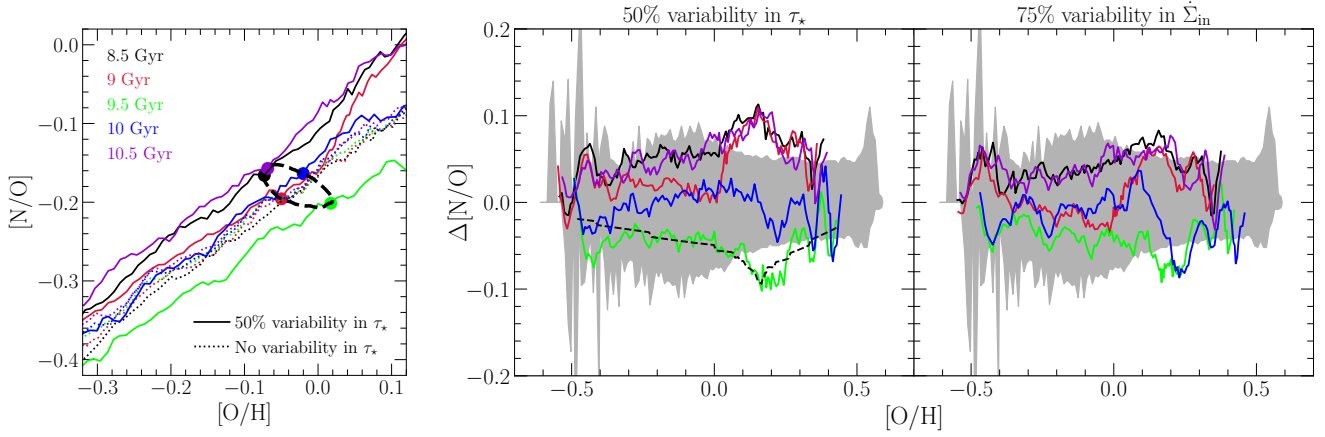
Figure 10. *Left*: One cycle of oscillations in the [N/O]-[O/H] relation at high [O/H] induced by sinusoidal variability in $\tau_\star$ with an amplitude of 0.5 (solid coloured lines; see equation 9). Dotted lines show the [N/O]-[O/H] relation at the same five snapshots in the fiducial model with no variability in $\tau_\star$ but still with diffusion migration (see discussion in § 3). The black dashed line shows the time evolution of the abundances at $R_{\rm gal}$ = 8 kpc, the approximate Galactocentric radius of the sun, with the times of each of the five snapshots marked by a coloured point. **Middle and Right**: For the same five snapshots in the left hand panel, the deviation in [N/O] at fixed [O/H] relative to the fiducial model for the case with sinusoidal variability in $\tau_\star$ at an amplitude of 0.5 (middle; see equation 9) and with sinusoidal variability in $\dot{\Sigma}_\star$ at an amplitude of 0.75 (right; see equation 10). The shaded regions in both panels quantify the width of the [N/O] distribution in $10^{10.5} - 10^{11}$ M$_\odot$ galaxies in MaNGA taken from Schaefer et al. (2020). In bins of [O/H], we place the median [N/O] at Δ[N/O] = 0, and the lower (upper) envelope denotes the 16th (84th) percentile of the [N/O] distribution.

our model is appropriate for Milky Way mass galaxies, we focus our comparison on the $M_\star = 10^{10.5} - 10^{11}$ M$_\odot$ mass range (Licquia & Newman 2015), which cuts our sample sample to 197,787 individual N and O measurements from the MaNGA IFU spaxels. In narrow bins of [O/H], we then compute the 16th, 50th, and 84th percentiles of the [N/O] distribution. Placing the median [N/O] at Δ[N/O] = 0, the shaded regions above and below 0 in Fig. 10 denote the difference between 16th and 84th percentiles of the distribution in each [O/H] bin.

We compare both of our oscillatory variants to the width of the [N/O] distribution by over-plotting the difference in [N/O] at fixed [O/H] between our oscillatory models and their constant counterpart (i.e. the vertical offset between the solid and dotted lines in the left panel, and the equivalent thereof for the oscillatory $\dot{\Sigma}_{\rm in}$ model). Both models produce offsets in [N/O] at fixed [O/H] which, as discussed above, arise as consequences of dilution, and the offsets are generally consistent with the width of the relation derived observationally by Schaefer et al. (2020). This supports their argument that variations in the local SFE can drive intrinsic scatter in the [N/O]-[O/H] relation, but the effects of stellar migration are still non-negligible. We demonstrate this by comparing the green solid line in the middle panel for the T = 9.5 Gyr snapshot to the black dashed line denoting the same quantity with post-processing migration (see discussion in § 3). While some of the features in Δ[N/O] as a function of [O/H] can be attributed to the difference in GCE parameters, stellar migration affects [N/O] ratios with an amplitude of ∼0.05 dex (see also Fig. 5 and discussion in § 4.1). Although this is smaller than the impact of oscillations in either $\tau_\star$ or $\dot{\Sigma}_{\rm in}$ (∼0.1 dex), it is nonetheless significant compared to the width of the Schaefer et al. (2020) distributions, also at the ≲0.1 dex level; this suggests that stellar migration is a subdominant but non-negligible source of scatter.

In general, variability in $\tau_\star$ impacts abundances more strongly than variability in $\dot{\Sigma}_{\rm in}$. Fig. 10 shows similar changes in [N/O] at fixed [O/H] in both of our oscillatory variants, but it requires an amplitude of 75% in accretion rates to achieve the same Δ[N/O] as an amplitude of 50% in the SFE. This arises out of an abun-

dance response which is much more *along* the [N/O]-[O/H] relation rather than *against* it as in the oscillatory $\tau_\star$ model (see the black dashed line in the left panel of Fig. 10). Both [O/H] and [N/H] vary with larger amplitudes in the variable infall model due to episodes of enhanced and suppressed accretion, but the effects of dilution on [N/H] are exacerbated by this in combination with metallicity dependent yields. As a result, [N/H] varies with a larger amplitude than [O/H], whereas the opposite is the case in the oscillatory $\tau_\star$ model. Consequently, [N/O] increases rather than decreases with increasing [O/H], and changes in [N/O] at fixed [O/H] are smaller. In the context of the observational results (Schaefer et al. 2020), this suggests that different [N/O] ratios at fixed [O/H] are less likely to reflect changes in the accretion rate and more likely to reflect variations in the internal properties of the star forming ISM, such as the thermal state or the pressure, quantities which here get folded into $\tau_\star$.

5 CONCLUSIONS

We have made use of the GCE models from Johnson et al. (2021) which characterize the Milky Way disc as a series of concentric rings with a uniform width $\delta R_{\rm gal}$ = 100 pc. As in previous models with similar motivations (Matteucci & Francois 1989; Wyse & Silk 1989; Prantzos & Aubert 1995; Schönrich & Binney 2009; Minchev et al. 2013, 2014, 2017; Sharma et al. 2021), this model treats each individual ring as a conventional one-zone model of chemical evolution. The novel addition to this model, however, is that it takes into account the impact that radial migration has on enrichment rates by allowing stellar populations to enrich distributions of radii as they migrate. We retained the IMF-averaged SN yields of O and Fe from Johnson et al. (2021), who in turn base these values off of Weinberg et al. (2017) and Johnson & Weinberg (2020). Assuming that the N yield from SNe Ia is negligible, we have investigated theoretical and empirical N yields from both massive stars and AGB stars.

If our fiducial CCSN yield of O is accurate ($y_{\rm O}^{\rm CC}$ = 0.015), then the CCSN yield of N required to reproduce the "plateau"

of $[N/O]_{cc} = -0.7$ at low $[O/H]$ is $y_N^{CC} = 3.6 \times 10^{-4}$. These values of both y_N^{CC} and $[N/O]_{cc}$ are consistent with the rotating CCSN models of Limongi & Chieffi (2018). N yields computed for non-rotating, lower metallicity progenitors are much smaller than their rotating counterparts (see Fig. 2; Woosley & Weaver 1995; Nomoto et al. 2013; Sukhbold et al. 2016; Limongi & Chieffi 2018). This suggests that the effects of rotation are necessary to explain the N abundances seen at low $[O/H]$, consistent with recent arguments from Grisoni et al. (2021).

Various AGB star nucleosynthesis models predict qualitatively different yields of N as a function of progenitor mass and metallicity (see Fig. 3). Ascertaining the origin of these differences is difficult because each model folds in different assumptions regarding important evolutionary parameters such as mass loss, opacities of various isotopic species, convection and convective boundaries, and nuclear reaction networks (see discussion in, e.g., § 5 of Karakas & Lugaro 2016). Nonetheless the differences between yield models can be qualitatively understood by considering the differences between how TDU and HBB proceed in the stellar models. In general, the most efficient N production occurs when both TDU and HBB occur simultaneously because each replenishment of C and O isotopes from the stellar core by TDU add new seed nuclei for HBB to process into ^{14}N via the CNO cycle (Ventura et al. 2013). Different assumptions regarding mass loss and opacity can also impact the duration of a star's AGB phase, inducing secondary effects on the N yields.

Similar to previous theoretical arguments regarding the low $[\alpha/Fe]$ stars in the Milky Way disc (e.g. Schönrich & Binney 2009; Nidever et al. 2014; Buck 2020; Sharma et al. 2021; Johnson et al. 2021), we find that with a smooth SFH the $[N/O]$-$[O/H]$ relation arises not out of an evolutionary sequence but as a superposition of endpoints. That is, the time evolution of each Galactic region through the $[N/O]$-$[O/H]$ plane is not the same line as the $[N/O]$-$[O/H]$ relation that would be observed at the present day in our model Galaxy (see Fig. 5). We additionally find that our model predicts the gas-phase $[N/O]$-$[O/H]$ relation to be relatively time-independent up to lookback times of $\sim 6-8$ Gyr, consistent with previous arguments that the relation is largely redshift-independent (Vincenzo & Kobayashi 2018; Hayden-Pawson et al. 2021).

Our fiducial model uses AGB star yields which are linear in both mass and metallicity with a slope of $\xi = 9 \times 10^{-4}$ (see equation 3). This is a factor of $2-3$ higher than the C11+C15 and V13 yields, but with a similar metallicity dependence. The fiducial model successfully reproduces the $[N/O]$-$[O/H]$ relation as observed, but the C11+C15 and V13 yield models require an artificial amplification by factors of 3 and 2, respectively. However, these yield models are successful if we instead simultaneously lower our SN yields from Johnson et al. (2021) and the outflow mass loading factor η at all radii by similar factors (see Fig. 6). This is physically plausible if a substantial fraction of high mass stars collapse to black holes instead of ending their lives as CCSNe. Although there is presently no combination of a massive star nucleosynthesis model and a physically motivated black hole landscape able to reproduce the observed abundance patterns (Griffith et al. 2021a), extensive black hole formation still lowers SN yields by simply robbing the yield of the ejecta from stars of various initial masses. This suggests that either N nucleosynthesis in AGB stars must be more efficient or that a substantial fraction of $M \gtrsim 8\ M_\odot$ stars must produce failed supernova; the answer may also be a combination of the two.

With both the K10 and KL16+K18 AGB star yields, our model is unable to reproduce the monotonic increase of $[N/O]$ with $[O/H]$ as

observed. This discrepancy persists if we consider alternate parameterizations of the CCSN yield of N as suggested by the non-rotating models of Woosley & Weaver (1995), Nomoto et al. (2013), Sukhbold et al. (2016), and Limongi & Chieffi (2018). In general, we find that reproducing the $[N/O]$-$[O/H]$ relation requires the total N yield from CCSNe and AGB stars to scale roughly linearly with the progenitor metallicity Z. Our model has sufficient success modeling the primary component of the N yield as a metallicity independent y_N^{CC} as suggested by CCSN models with rotating progenitors and a secondary component described by an AGB star yield of N which scales roughly linearly with Z, but there is some room for trade-off between these two enrichment channels because our model best constrains the sum of the two. Our linear yield model as well as the C11+C15 and V13 models qualitatively reproduce this scaling, which we illustrate in Fig. 4. The normalization of the AGB star yields, however, depends on the SN yields and the efficiency of outflows as discussed in § 4.2.

To test our model against N abundances observed in stars, we make use of the measurements presented in Vincenzo et al. (2021) with asteroseismic mass measurements. To estimate birth abundances of N, they use MESA stellar evolution models (Paxton et al. 2011, 2013, 2015, 2018) to correct the spectroscopically derived measurements for internal mixing processes known to affect the photospheric abundances of N in evolved stars (i.e. dredge-up of CNO cycle products; Gilroy 1989; Korn et al. 2007; Lind et al. 2008; Souto et al. 2018, 2019). They find that $[N/O]$ at fixed $[Fe/H]$ is relatively age-independent, a result which our model successfully reproduces (see Fig. 9). This is a notable success of our model and the Vincenzo et al. (2021) estimates because with uncorrected N abundances, $[N/O]$ at fixed $[Fe/H]$ shows an inverse dependence on stellar age (see their Fig. 7). Additionally, our model predicts $[N/O]$ to increase with decreasing $[O/Fe]$ in agreement with Vincenzo et al. (2021). This suggests that the chemical dichotomy between the thin and thick discs persists even when using birth abundances of N (for details on the Galaxy's two chemical populations, see discussion in, e.g., Hayden et al. 2015; Weinberg et al. 2019, 2021; Griffith et al. 2021b). Both of these results arise out of a correlation between $[N/H]$ and $[Fe/H]$ in the ISM predicted by the model, whereas the relation between $[N/H]$ and $[O/H]$ is much weaker up to lookback times of ~10 Gyr. This gives rise to both the flat nature of the $[N/O]$-age relation at fixed $[Fe/H]$ and the inverse relationship between $[N/O]$ and $[O/Fe]$ (see Fig. 9 and discussion in § 4.4).

To investigate the sources of scatter in the $[N/O]$-$[O/H]$ relation, we construct two variations of the fiducial model from Johnson et al. (2021). In these alternate scenarios, we specify the accretion history of the Galaxy rather than the star formation history and impose sinusoidal oscillations on either the SFE or the accretion history itself. We choose an amplitude of 50% in the SFE because it is comparable to the observationally derived scatter in molecular gas depletion times (Tacconi et al. 2018). We set the amplitude to 75% for our oscillatory accretion history model because the resultant variability in the SFR is of similar magnitude to the variable SFE model (~40%). In general, we find that these oscillations induce variability in the gas-phase $[N/O]$ ratio at fixed $[O/H]$ that is a factor of ~2 larger than that caused by stellar migration. This is a consequence of the quick production timescale of N by single stellar populations (~ 250 Myr, see Fig. 4 and discussion in § 2.3): there simply is not much time for orbits to dynamically evolve before most of a stellar population's N is ejected to the ISM. Our oscillatory models predict changes in $[N/O]$ at fixed $[O/H]$ that are comparable to the scatter in the relation derived observationally by Schaefer et al. (2020) using data from the MaNGA IFU survey (Bundy et al. 2015). They demonstrate that this scatter is correlated with variations in the local SFE, with lower SFE system

exhibiting higher [N/O] at fixed [O/H]. Our chemical evolution models successfully reproduce this result, additionally suggesting that migration plays a sub-dominant but nonetheless significant role in driving scatter in the [N/O]-[O/H] relation.

When weighted by the IMF (Kroupa 2001), the C11+C15 yields predict roughly equal contributions per linear dM_{ZAMS} interval. Each additional model shows a substantially higher contribution from AGB stars with masses of $\gtrsim 3$ $M_\odot$. In all cases, the characteristic delay times for production by single stellar populations are $\lesssim 250$ Myr. This is true even for the C11+C15 yields because of the steep nature of the stellar mass-lifetime relation: most of the mass range of stars that will go through an AGB phase within the age of the universe will do so within a few hundred Myr of their formation. The DTD of N production by AGB stars is therefore quite prompt, and although it does affect the stellar abundances (see discussion in § 4.4), the metallicity dependence plays a much larger role in establishing the [N/O]-[O/H] relation as observed. Due to the relatively prompt nature of N enrichment, stellar migration has a minimal impact on N enrichment rates. As demonstrated in § 4.5 in comparison to the measurements by Schaefer et al. (2020), they impact the gas-phase [N/O] ratio at only the ~0.05 dex level. If the DTD were more extended, there would be more time for dynamical evolution before nucleosynthetic products are deposited to the ISM, and migration would consequently have a more substantial impact on enrichment rates; this indeed appears to be the case for SN Ia production of Fe (see discussion in § 4.1 and in §§ 3.1 and 3.4 of Johnson et al. 2021).

The results outlined in this paper highlight the importance of empirically calibrated yields of all elements from all nucleosynthetic sources in GCE models. The combination of theoretically predicted yields and flexible computational tools such as VICE can provide powerful constraints for future models of elemental production and galaxy evolution. When future spectroscopic surveys begin collecting data, studies such as this will be essential to illuminating the lessons they can teach us about the history of nuclear reactions in our home Galaxy.

REFERENCES

Adams S. M., Kochanek C. S., Gerke J. R., Stanek K. Z., Dai X., 2017, MNRAS, 468, 4968

Anders E., Grevesse N., 1989, Geochimica Cosmochimica Acta, 53, 197

Andrews B. H., Martini P., 2013, ApJ, 765, 140

Andrews B. H., Weinberg D. H., Schönrich R., Johnson J. A., 2017, ApJ, 835, 224

Asplund M., Grevesse N., Sauval A. J., 2005, in Barnes Thomas G. I., Bash F. N., eds, Astronomical Society of the Pacific Conference Series Vol. 336, Cosmic Abundances as Records of Stellar Evolution and Nucleosynthesis. p. 25

Asplund M., Grevesse N., Sauval A. J., Scott P., 2009, ARA&A, 47, 481

Asplund M., Amarsi A. M., Grevesse N., 2021, A&A, 653, A141

Basinger C. M., Kochanek C. S., Adams S. M., Dai X., Stanek K. Z., 2021, MNRAS, 508, 1156

Belfiore F., et al., 2017, MNRAS, 469, 151

Berg D. A., et al., 2012, ApJ, 754, 98

Berg D. A., Skillman E. D., Croxall K. V., Pogge R. W., Moustakas J., Johnson-Groh M., 2015, ApJ, 806, 16

Berg D. A., Pogge R. W., Skillman E. D., Croxall K. V., Moustakas J., Rogers N. S. J., Sun J., 2020, ApJ, 893, 96

Bigiel F., Leroy A., Walter F., Blitz L., Brinks E., de Blok W. J. G., Madore B., 2010, AJ, 140, 1194

Bilitewski T., Schönrich R., 2012, MNRAS, 426, 2266

Bird J. C., Kazantzidis S., Weinberg D. H., 2012, MNRAS, 420, 913

Bird J. C., Loebman S. R., Weinberg D. H., Brooks A. M., Quinn T. R., Christensen C. R., 2021, MNRAS, 503, 1815

Bland-Hawthorn J., Gerhard O., 2016, ARA&A, 54, 529

Bloecker T., 1995, A&A, 297, 727

Bovy J., Leung H. W., Hunt J. A. S., Mackereth J. T., García-Hernández D. A., Roman-Lopes A., 2019, MNRAS, 490, 4740

Brooks A. M., Zolotov A., 2014, ApJ, 786, 87

Brooks A. M., Papastergis E., Christensen C. R., Governato F., Stilp A., Quinn T. R., Wadsley J., 2017, ApJ, 850, 97

Brunetti M., Chiappini C., Pfenniger D., 2011, A&A, 534, A75

Buck T., 2020, MNRAS, 491, 5435

Bundy K., et al., 2015, ApJ, 798, 7

Chiappini C., et al., 2015, A&A, 576, L12

Chieffi A., Limongi M., 2004, ApJ, 608, 405

Chieffi A., Limongi M., 2013, ApJ, 764, 21

Chisholm J., Tremonti C., Leitherer C., 2018, MNRAS, 481, 1690

Christensen C., Quinn T., Governato F., Stilp A., Shen S., Wadsley J., 2012, MNRAS, 425, 3058

Christensen C. R., Brooks A. M., Fisher D. B., Governato F., McCleary J., Quinn T. R., Shen S., Wadsley J., 2014a, MNRAS, 440, L51

Christensen C. R., Governato F., Quinn T., Brooks A. M., Shen S., McCleary J., Fisher D. B., Wadsley J., 2014b, MNRAS, 440, 2843

Christensen C. R., Davé R., Governato F., Pontzen A., Brooks A., Munshi F., Quinn T., Wadsley J., 2016, ApJ, 824, 57

Christensen C. R., Davé R., Brooks A., Quinn T., Shen S., 2018, ApJ, 867, 142

Conroy C., 2013, ARA&A, 51, 393

Conroy C., Graves G. J., van Dokkum P. G., 2014, ApJ, 780, 33

Cristallo S., et al., 2011, ApJS, 197, 17

Cristallo S., Straniero O., Piersanti L., Gobrecht D., 2015, ApJS, 219, 40

David L. P., Forman W., Jones C., 1990, ApJ, 359, 29

de los Reyes M. A. C., Kennicutt Robert C. J., 2019, ApJ, 872, 16

Doherty C. L., Gil-Pons P., Siess L., Lattanzio J. C., 2017, Publ. Astron. Soc. Australia, 34, e056

Dopita M. A., Kewley L. J., Sutherland R. S., Nicholls D. C., 2016, Ap&SS, 361, 61

El-Badry K., Wetzel A., Geha M., Hopkins P. F., Kereš D., Chan T. K., Faucher-Giguère C.-A., 2016, ApJ, 820, 131

Ellison S. L., Lin L., Thorp M. D., Pan H.-A., Scudder J. M., Sánchez S. F., Bluck A. F. L., Maiolino R., 2021, MNRAS, 501, 4777

Ertl T., Janka H. T., Woosley S. E., Sukhbold T., Ugliano M., 2016, ApJ, 818, 124

Frankel N., Rix H.-W., Ting Y.-S., Ness M., Hogg D. W., 2018, ApJ, 865, 96

Frankel N., Sanders J., Rix H.-W., Ting Y.-S., Ness M., 2019, ApJ, 884, 99

Frischknecht U., et al., 2016, MNRAS, 456, 1803

Gallino R., Arlandini C., Busso M., Lugaro M., Travaglio C., Straniero O., Chieffi A., Limongi M., 1998, ApJ, 497, 388

Gerke J. R., Kochanek C. S., Stanek K. Z., 2015, MNRAS, 450, 3289
Gil-Pons P., Doherty C. L., Lau H., Campbell S. W., Suda T., Guilani S., Gutiérrez J., Lattanzio J. C., 2013, A&A, 557, A106
Gil-Pons P., Doherty C. L., Gutiérrez J., Campbell S. W., Siess L., Lattanzio J. C., 2021, A&A, 645, A10
Gilroy K. K., 1989, ApJ, 347, 835
Governato F., et al., 2012, MNRAS, 422, 1231
Grevesse N., Sauval A. J., 1998, Space Sci. Rev., 85, 161
Griffith E. J., Sukhbold T., Weinberg D. H., Johnson J. A., Johnson J. W., Vincenzo F., 2021a, arXiv e-prints, p. arXiv:2103.09837
Griffith E. J., Weinberg D. H., Buder S., Johnson J. A., Johnson J. W., Vincenzo F., 2021b, arXiv e-prints, p. arXiv:2110.06240
Grisoni V., Matteucci F., Romano D., 2021, MNRAS, 508, 719
Gronow S., Cote B., Lach F., Seitenzahl I. R., Collins C. E., Sim S. A., Roepke F. K., 2021a, arXiv e-prints, p. arXiv:2103.14050
Gronow S., Collins C. E., Sim S. A., Röpke F. K., 2021b, A&A, 649, A155
Hayden-Pawson C., et al., 2021, arXiv e-prints, p. arXiv:2110.00033
Hayden M. R., et al., 2015, ApJ, 808, 132
Heger A., Woosley S. E., 2010, ApJ, 724, 341
Hekker S., Johnson J. A., 2019, MNRAS, 487, 4343
Henry R. B. C., Worthey G., 1999, PASP, 111, 919
Henry R. B. C., Edmunds M. G., Köppen J., 2000, ApJ, 541, 660
Hopkins P. F., Kereš D., Oñorbe J., Faucher-Giguère C.-A., Quataert E., Murray N., Bullock J. S., 2014, MNRAS, 445, 581
Hurley J. R., Pols O. R., Tout C. A., 2000, MNRAS, 315, 543
Izotov Y. I., Thuan T. X., Guseva N. G., 2012, A&A, 546, A122
Izzard R. G., Preece H., Jofre P., Halabi G. M., Masseron T., Tout C. A., 2018, MNRAS, 473, 2984
James B. L., Koposov S., Stark D. P., Belokurov V., Pettini M., Olszewski E. W., 2015, MNRAS, 448, 2687
Jenkins A., 1992, MNRAS, 257, 620
Jenkins A., Binney J., 1990, MNRAS, 245, 305
Jofré P., et al., 2016, A&A, 595, A60
Johnson J. A., 2019, Science, 363, 474
Johnson J. W., Weinberg D. H., 2020, MNRAS, 498, 1364
Johnson J. W., et al., 2021, MNRAS, 508, 4484
Karakas A. I., 2010, MNRAS, 403, 1413
Karakas A. I., Lugaro M., 2016, ApJ, 825, 26
Karakas A. I., Lugaro M., Carlos M., Cseh B., Kamath D., García-Hernández D. A., 2018, MNRAS, 477, 421
Kennicutt Robert C. J., 1998, ApJ, 498, 541
Kennicutt R. C., Evans N. J., 2012, ARA&A, 50, 531
Kennicutt Robert C. J., de los Reyes M. A. C., 2021, ApJ, 908, 61
Kobayashi C., 2004, MNRAS, 347, 740
Kodama T., Arimoto N., 1997, A&A, 320, 41
Korn A. J., Grundahl F., Richard O., Mashonkina L., Barklem P. S., Collet R., Gustafsson B., Piskunov N., 2007, ApJ, 671, 402
Kroupa P., 2001, MNRAS, 322, 231
Krumholz M. R., Burkhart B., Forbes J. C., Crocker R. M., 2018, MNRAS, 477, 2716
LUNA Collaboration et al., 2006, Physics Letters B, 634, 483
Lacey C. G., Fall S. M., 1985, ApJ, 290, 154
Lagarde N., Decressin T., Charbonnel C., Eggenberger P., Ekström S., Palacios A., 2012, A&A, 543, A108
Larson R. B., 1974, MNRAS, 166, 585
Law D. R., Majewski S. R., 2010, ApJ, 714, 229
Leroy A. K., Walter F., Brinks E., Bigiel F., de Blok W. J. G., Madore B., Thornley M. D., 2008, AJ, 136, 2782
Leroy A. K., et al., 2013, AJ, 146, 19
Licquia T. C., Newman J. A., 2015, ApJ, 806, 96
Limongi M., Chieffi A., 2018, ApJS, 237, 13
Lind K., Korn A. J., Barklem P. S., Grundahl F., 2008, A&A, 490, 777
Liu L., Gao Y., Greve T. R., 2015, ApJ, 805, 31
Lodders K., 2003, ApJ, 591, 1220
Maeder A., Meynet G., 1989, A&A, 210, 155
Maeder A., Zahn J.-P., 1998, A&A, 334, 1000
Maiolino R., Mannucci F., 2019, A&ARv, 27, 3
Majewski S. R., et al., 2017, AJ, 154, 94

Marigo P., 2002, A&A, 387, 507
Martig M., et al., 2015, MNRAS, 451, 2230
Martig M., et al., 2016, MNRAS, 456, 3655
Matteucci F., Francois P., 1989, MNRAS, 239, 885
Miglio A., et al., 2021, A&A, 645, A85
Mihalas D., Binney J., 1981, Galactic astronomy. Structure and kinematics
Minchev I., Famaey B., Combes F., Di Matteo P., Mouhcine M., Wozniak H., 2011, A&A, 527, A147
Minchev I., Chiappini C., Martig M., 2013, A&A, 558, A9
Minchev I., Chiappini C., Martig M., 2014, A&A, 572, A92
Minchev I., Steinmetz M., Chiappini C., Martig M., Anders F., Matijevic G., de Jong R. S., 2017, ApJ, 834, 27
Mollá M., Vílchez J. M., Gavilán M., Díaz A. I., 2006, MNRAS, 372, 1069
Munshi F., et al., 2013, ApJ, 766, 56
Nidever D. L., et al., 2014, ApJ, 796, 38
Nomoto K., Kobayashi C., Tominaga N., 2013, ARA&A, 51, 457
Padovani P., Matteucci F., 1993, ApJ, 416, 26
Paxton B., Bildsten L., Dotter A., Herwig F., Lesaffre P., Timmes F., 2011, ApJS, 192, 3
Paxton B., et al., 2013, ApJS, 208, 4
Paxton B., et al., 2015, ApJS, 220, 15
Paxton B., et al., 2018, ApJS, 234, 34
Pejcha O., Thompson T. A., 2015, ApJ, 801, 90
Pérez-Montero E., Contini T., 2009, MNRAS, 398, 949
Pilyugin L. S., Vílchez J. M., Thuan T. X., 2010, ApJ, 720, 1738
Pilyugin L. S., Grebel E. K., Mattsson L., 2012, MNRAS, 424, 2316
Prantzos N., Aubert O., 1995, A&A, 302, 69
Rogers N. S. J., Skillman E. D., Pogge R. W., Berg D. A., Moustakas J., Croxall K. V., Sun J., 2021, ApJ, 915, 21
Sánchez S. F., 2020, ARA&A, 58, 99
Schaefer A. L., Tremonti C., Belfiore F., Pace Z., Bershady M. A., Andrews B. H., Drory N., 2020, ApJ, 890, L3
Schiavon R. P., 2010, Publication of Korean Astronomical Society, 25, 83
Schönrich R., Binney J., 2009, MNRAS, 396, 203
Sellwood J. A., Binney J. J., 2002, MNRAS, 336, 785
Sharma S., Hayden M. R., Bland-Hawthorn J., 2021, MNRAS, 507, 5882
Silva Aguirre V., et al., 2018, MNRAS, 475, 5487
Skillman E. D., Berg D. A., Pogge R. W., Moustakas J., Rogers N. S. J., Croxall K. V., 2020, ApJ, 894, 138
Souto D., et al., 2018, ApJ, 857, 14
Souto D., et al., 2019, ApJ, 874, 97
Spitoni E., Silva Aguirre V., Matteucci F., Calura F., Grisoni V., 2019, A&A, 623, A60
Spitoni E., et al., 2021, A&A, 647, A73
Sukhbold T., Ertl T., Woosley S. E., Brown J. M., Janka H. T., 2016, ApJ, 821, 38
Suliga A. M., Shalgar S., Fuller G. M., 2021, J. Cosmology Astropart. Phys., 2021, 042
Tacconi L. J., et al., 2018, ApJ, 853, 179
van Zee L., Salzer J. J., Haynes M. P., 1998, ApJ, 497, L1
Vassiliadis E., Wood P. R., 1993, ApJ, 413, 641
Ventura P., Di Criscienzo M., Carini R., D'Antona F., 2013, MNRAS, 431, 3642
Ventura P., di Criscienzo M., D'Antona F., Vesperini E., Tailo M., Dell'Agli F., D'Ercole A., 2014, MNRAS, 437, 3274
Ventura P., Karakas A., Dell'Agli F., García-Hernández D. A., Guzman-Ramirez L., 2018, MNRAS, 475, 2282
Ventura P., Dell'Agli F., Lugaro M., Romano D., Tailo M., Yagüe A., 2020, A&A, 641, A103
Vila-Costas M. B., Edmunds M. G., 1993, MNRAS, 265, 199
Vincenzo F., Kobayashi C., 2018, MNRAS, 478, 155
Vincenzo F., Kobayashi C., 2020, MNRAS, 496, 80
Vincenzo F., Belfiore F., Maiolino R., Matteucci F., Ventura P., 2016a, MNRAS, 458, 3466
Vincenzo F., Matteucci F., de Boer T. J. L., Cignoni M., Tosi M., 2016b, MNRAS, 460, 2238
Vincenzo F., et al., 2021, arXiv e-prints, p. arXiv:2106.03912
Wadsley J. W., Stadel J., Quinn T., 2004, New Astron., 9, 137

Warfield J. T., et al., 2021, AJ, 161, 100
Weinberg D. H., Andrews B. H., Freudenburg J., 2017, ApJ, 837, 183
Weinberg D. H., et al., 2019, ApJ, 874, 102
Weinberg D. H., et al., 2021, arXiv e-prints, p. arXiv:2108.08860
Woosley S. E., Weaver T. A., 1995, ApJS, 101, 181
Wyse R. F. G., Silk J., 1989, ApJ, 339, 700
Yong D., et al., 2016, MNRAS, 459, 487
Zahn J. P., 1992, A&A, 265, 115
Zolotov A., et al., 2012, ApJ, 761, 71

Appendices

A VICE

VICE[1] is an open-source PYTHON package designed to model chemical enrichment processes in galaxies with a generic, flexible model. With this paper, we mark the release of version 1.3.0 which presents a handful of new features:

(i) Users may select a mass-lifetime relation for stars from a list of several parameterized forms taken from the literature. Previously, only a single power-law was implemented, but this formulation underestimates lifetimes for stars with masses $\gtrsim 4 M_\odot$; now, the options include the equations presented in:

- Vincenzo et al. (2016b)
- Hurley, Pols & Tout (2000)
- Kodama & Arimoto (1997)
- Padovani & Matteucci (1993)
- Maeder & Meynet (1989)
- Larson (1974) **(default)**

Generally, chemical evolution models make similar predictions with each of these different forms of the mass-lifetime relation since they are not considerably different from one another (see the section titled "Single Stellar Populations" under VICE's science documentation for further discussion[2]). We select the Larson (1974) form as a default within VICE because it is representative of other forms and requires the lowest amount of computational overhead (aside from the single power-law option). This model is a parabola in $\log \tau - \log m$ space for which we take updated coefficients from Kobayashi (2004) and David et al. (1990).

(ii) We have added two additional tables of AGB star yields sampled at various progenitor masses and metallicities: the KL16+K18 and V13 models presented in this paper are new to VICE (see discussion in § 2.2 for details).

(iii) We have built in the SN Ia yields presented in Gronow et al. (2021b,a). These tables present yields for double detonations of sub-Chandrasekhar mass carbon-oxygen white dwarfs at various progenitor metallicities.

Although VICE includes built-in SN and AGB star yield tables, users are not required to adopt any one of them for use in their chemical evolution models. Instead, it allows arbitrary functions of metallicity for both CCSN and SN Ia yields and functions of progenitor mass and metallicity for AGB star yields. It provides similar flexibility for additional parameters typically built into GCE models. VICE's backend is implemented entirely in ANSI/ISO C, providing it with the powerful computing speeds of a compiled library while retaining such scientific flexibility within the easy-to-use framework of PYTHON.

Requiring a Unix kernel, VICE supports Mac and Linux operating systems; Windows users should install and use VICE entirely within the Windows Subsystem for Linux. On machines with x86_64 hardware, it can be installed in a terminal via `pip install vice`. Users running ARM64 hardware (e.g. Macintosh computers with Apple's new M1 processor) must install VICE by compiling from source, instructions for which can be found in the documentation. After installing, running `vice --docs` and `vice --tutorial` from a Unix terminal will launch a web browser to the documentation and to a jupyter notebook intended to familiarize first time users with VICE's API.

---

[1] Install (PyPI): https://pypi.org/project/vice
Documentation: https://vice-astro.readthedocs.io
Source Code: https://github.com/giganano/VICE.git
[2] https://vice-astro.readthedocs.io/en/latest/science_documentation/